



HAL
open science

Estimating the atmospheric properties of 44 M dwarfs from SPIRou spectra

P Cristofari, J-F Donati, T Masseron, P Fouqué, C Moutou, A Carmona, E
Artigau, E Martioli, G Hébrard, E Gaidos, et al.

► **To cite this version:**

P Cristofari, J-F Donati, T Masseron, P Fouqué, C Moutou, et al.. Estimating the atmospheric properties of 44 M dwarfs from SPIRou spectra. *Monthly Notices of the Royal Astronomical Society*, 2022, 516 (3), pp.3802-3820. 10.1093/mnras/stac2364 . hal-03827438

HAL Id: hal-03827438

<https://hal.science/hal-03827438v1>

Submitted on 6 Jul 2023

HAL is a multi-disciplinary open access archive for the deposit and dissemination of scientific research documents, whether they are published or not. The documents may come from teaching and research institutions in France or abroad, or from public or private research centers.

L'archive ouverte pluridisciplinaire **HAL**, est destinée au dépôt et à la diffusion de documents scientifiques de niveau recherche, publiés ou non, émanant des établissements d'enseignement et de recherche français ou étrangers, des laboratoires publics ou privés.

Estimating the atmospheric properties of 44 M dwarfs from SPIRou spectra

P. I. Cristofari¹,¹★ J.-F. Donati¹,¹ T. Masseron,^{2,3} P. Fouqué,^{1,4} C. Moutou,¹ A. Carmona,⁵ E. Artigau,⁶ E. Martioli,^{7,8} G. Hébrard,^{7,9} E. Gaidos¹⁰,¹⁰ X. Delfosse⁵ and the SLS consortium

¹Université de Toulouse, CNRS, IRAP, 14 av. Belin, F-31400 Toulouse, France

²Instituto de Astrofísica de Canarias, E-38205 La Laguna, Tenerife, Spain

³Departamento de Astrofísica, Universidad de La Laguna, E-38206 La Laguna, Tenerife, Spain

⁴Canada–France–Hawaii Telescope, CNRS, Kamuela, HI 96743, USA

⁵Université Grenoble Alpes, CNRS, IPAG, F-38000 Grenoble, France

⁶Département de Physique, Université de Montréal, IREX, Montréal, QC H3C 3J7, Canada

⁷Institut d'Astrophysique de Paris, CNRS, UMR 7095, Sorbonne Université, F-75014 Paris, France

⁸Laboratório Nacional de Astrofísica, Itajubá, MG 37504-364, Brazil

⁹Observatoire de Haute Provence, CNRS, Université d'Aix-Marseille, F-04870 Saint-Michel-l'Observatoire, France

¹⁰Department of Earth Sciences, University of Hawai'i at Mānoa, Honolulu, HI 96822, USA

Accepted 2022 August 18. Received 2022 August 12; in original form 2022 June 17

ABSTRACT

We describe advances on a method designed to derive accurate parameters of M dwarfs. Our analysis consists in comparing high-resolution infrared spectra acquired with the near-infrared spectro-polarimeter SPIRou to synthetic spectra computed from MARCS model atmospheres, in order to derive the effective temperature (T_{eff}), surface gravity ($\log g$), metallicity ($[M/H]$), and alpha-enhancement ($[\alpha/Fe]$) of 44 M dwarfs monitored within the SPIRou Legacy Survey (SLS). Relying on 12 of these stars, we calibrated our method by refining our selection of well-modelled stellar lines, and adjusted the line list parameters to improve the fit when necessary. Our retrieved T_{eff} , $\log g$, and $[M/H]$ are in good agreement with literature values, with dispersions of the order of 50 K in T_{eff} and 0.1 dex in $\log g$ and $[M/H]$. We report that fitting $[\alpha/Fe]$ has an impact on the derivation of the other stellar parameters, motivating us to extend our fitting procedure to this additional parameter. We find that our retrieved $[\alpha/Fe]$ are compatible with those expected from empirical relations derived in other studies.

Key words: techniques: spectroscopic – stars: fundamental parameters – stars: low-mass – infrared: stars.

1 INTRODUCTION

M dwarfs are obvious targets of interest to look for exoplanets, especially those located in the habitable zones of their host stars (Bonfils et al. 2013; Dressing & Charbonneau 2013; Gaidos et al. 2016), as they dominate the stellar population of the solar neighbourhood. In order to accurately characterize these planets, and derive their masses and radii, it is essential to obtain reliable estimates of the fundamental parameters of the host stars. In particular, the effective temperature (T_{eff}), surface gravity ($\log g$), and overall metallicity ($[M/H]$) of M dwarfs must be determined as accurately as possible.

Several techniques have been developed to characterize atmospheric parameters of low-mass stars. Some rely on the adjustment of equivalent widths (Rojas-Ayala et al. 2010; Neves et al. 2014; Fouqué et al. 2018). Others attempt to fit spectral energy distributions (SEDs) on low- to mid-resolution spectra (Mann et al. 2013). More recently, advances in spectral modelling and the advent of new high-resolution spectrographs in the near-infrared (NIR) domain allowed some authors to perform direct fits of synthetic spectra on

high-resolution spectroscopic observations (Passegger et al. 2018; Schweitzer et al. 2019; Marfil et al. 2021).

Of these techniques, the latter is presumably the best option to retrieve precise estimates of the atmospheric parameters by modelling individual spectral lines rather than integrated quantities such as equivalent width or bandpass fluxes. To succeed, this approach however requires accurate high-resolution synthetic spectra on the one hand, and high-resolution and high signal-to-noise ratio (SNR) spectroscopic observations on the other hand. To this end, model atmospheres of low-mass stars such as MARCS (Gustafsson et al. 2008), ATLAS (Kurucz 1970), or PHOENIX (Allard & Hauschildt 1995) were developed and refined over the last few decades. While PHOENIX also performs the radiative transfer to produce synthetic spectra, other codes are used to compute emergent spectra from model atmospheres, such as Turbospectrum (Alvarez & Plez 1998; Plez 2012) or SYNTHÉ (Kurucz 2005), in the case of MARCS and ATLAS atmospheric models, respectively. In parallel, instruments such as SPIRou (Donati et al. 2020), CARMENES (Quirrenbach et al. 2014), iSHELL (Rayner et al. 2016), IRD (Kotani et al. 2018), or HPF (Mahadevan et al. 2012) have provided the community with high-quality and high-resolution spectra in the NIR domain.

* E-mail: paul.cristofari@irap.omp.eu

For M dwarfs in the NIR domain, the modelling of stellar spectra is particularly challenging because of the high density of atomic and molecular lines, forming deep absorption bands. Furthermore, telluric features, extremely abundant in the NIR domain, often blend with stellar lines and forces one to carry out extra processing steps to extract the stellar spectrum. In spite of these challenges, the NIR domain remains an abundant source of information, particularly for M dwarfs that are brighter in the NIR than in the optical.

In this paper, we pursue the work initiated in Cristofari et al. (2022, hereafter C22) with the ultimate goal of providing the community with accurate stellar parameters for most M dwarfs observed with SPIRou. Over 70 of them have been monitored with this instrument in the context of the SPIRou Legacy Survey (SLS, Donati et al. 2020), an ongoing observation program for which 310 nights were allocated on the 3.6-m Canada–France–Hawaii Telescope (CFHT). M dwarfs within the SLS are typically monitored tens of times over successive seasons, allowing us to produce high-quality median spectra for our analysis (C22), which we call ‘template spectra’ in the following. In this work, we focus on the 44 M dwarfs that were most intensively observed with SPIRou.

In contrast with C22, we focus in this paper on MARCS model atmospheres to derive stellar parameters, and bring several improvements to our method. More specifically, we extend our tools to constrain the abundance of alpha elements (O, Ne, Mg, Si, S, Ar, Ca, and Ti) for the studied targets, and demonstrate the importance of considering the alpha-enhancement parameter ($[\alpha/\text{Fe}]$) when modelling spectra of M dwarfs.

In Section 2, we introduce the selected targets and the processing steps undertaken to produce template spectra from SPIRou observations. We recall the main steps of our analysis in Section 3 along with the implemented improvements. We then discuss the impact of $[\alpha/\text{Fe}]$ on the retrieved parameters in Section 4, outline the modifications brought to the parameters of some of the atomic lines used in our work (see Section 5), and present the results of our analysis of 44 M dwarfs in Section 6. We conclude and discuss the results of our work in Section 7.

2 OBSERVATIONS AND REDUCTION

2.1 Selecting targets

Most stars were monitored several tens of times over successive seasons with the widest possible range of Barycentric Earth Radial Velocities (BERV). In this work, we focus on 44 M dwarfs for which at least 20 SPIRou spectra were collected in order to build high-SNR stellar templates (see Section 2.2, Table 1). For now, we exclude highly active targets, for which stellar line profiles are likely to be impacted by magnetic fields and chromospheric activity. Several publications assessed the activity level from $H\alpha$ equivalent width for most targets of our sample (Fouqué et al. 2018; Schöfer et al. 2019), confirming that they are no more than weakly active. We further performed visual inspection of the spectra to ensure that the stellar lines were not significantly affected by activity, e.g. with core reversals in strong lines like those seen in the spectra of more active targets (such as GJ 3622).

Out of our 44 stars, we use 12 (the same as in C22, see Table 2) to improve our tools and calibrate our analysis procedure. We consider the parameters published by Mann et al. (2015, hereafter M15) as a reference for these stars, given that this study relies on methods that are largely independent from ours (e.g. SED fits to low-resolution spectra, equivalent widths, and empirical mass–magnitude relations), and agree well with other literature studies. Table 3 presents the stellar

Table 1. Number of spectra, visits, and typical SNR of the collected observations.

Star	Nb. spectra	Nb. epochs	Med. SNR [SNR range]
GI 338B	124	31	250 [150–300]
GI 410	472	112	130 [50–150]
GI 846	792	194	160 [50–230]
GI 205	593	143	290 [50–350]
GI 880	634	155	200 [70–250]
GI 514	740	152	160 [50–280]
GI 382	238	59	150 [50–220]
GI 412A	884	148	180 [60–350]
GI 15A	1040	198	280 [60–360]
GI 411	592	143	360 [200–440]
GI 752A	523	129	170 [50–230]
GI 48	786	195	130 [60–150]
GI 617B	546	133	120 [50–150]
GI 480	283	70	110 [60–120]
GI 436	188	38	150 [70–220]
GI 849	771	189	120 [50–140]
GI 408	495	117	140 [50–170]
GI 687	898	214	200 [60–240]
GI 725A	889	213	210 [50–260]
GI 317	108	27	100 [70–130]
GI 251	749	175	140 [50–170]
GJ 4063	784	190	100 [50–120]
GI 581	124	31	120 [60–150]
GI 725B	855	211	160 [70–200]
PM J09553–2715	172	43	110 [80–140]
GI 876	369	88	160 [70–220]
GJ 1012	522	129	100 [50–120]
GJ 4333	734	181	100 [50–120]
GI 445	171	43	110 [50–140]
GJ 1148	399	98	100 [50–110]
PM J08402+3127	462	115	100 [50–110]
GJ 3378	725	179	100 [50–130]
GJ 1105	515	128	100 [50–130]
GI 699	950	231	200 [60–240]
GI 169.1A	673	165	100 [50–130]
PM J21463+3813	718	177	100 [50–120]
GI 15B	755	188	100 [50–120]
GJ 1289	812	202	100 [50–110]
GI 447	180	45	120 [60–170]
GJ 1151	568	141	100 [50–120]
GJ 1103	254	62	100 [50–110]
GI 905	484	117	110 [50–130]
GJ 1002	524	130	100 [60–120]
GJ 1286	438	113	100 [50–120]

parameters for 16 additional stars included in our sample for which M15 reported stellar properties.

2.2 Building templates from SPIRou spectra

All SPIRou spectra are processed through the SPIRou reduction pipeline, APERO (version 0.6.132, Cook et al., in preparation). A correction of the telluric absorption and emission lines is performed by APERO, relying on telluric templates built from telluric standards (Artigau et al., in preparation). A blaze profile estimated from flat-field exposures is used to flatten the extracted spectra, and each order is normalized using a third-degree polynomial.

Stellar templates are built by taking the median of the telluric corrected spectra in the barycentric reference frame. Because of the relative motion of telluric lines with respect to spectral features due to the Earth revolution around the Sun, having spectra observed at

Table 2. Parameters derived by M15 for 12 calibration stars used in this study. $\log g$ values are computed from reported masses and radii.

Star	Spectral type	T_{eff}	[M/H]	Radius	Mass	$\log g$
Gl 846	M0.5V	3848 ± 60	0.02 ± 0.08	0.546 ± 0.019	0.590 ± 0.059	4.74 ± 0.05
Gl 880	M1.5V	3720 ± 60	0.21 ± 0.08	0.549 ± 0.018	0.574 ± 0.057	4.72 ± 0.05
Gl 15A	M2V	3603 ± 60	-0.30 ± 0.08	0.388 ± 0.013	0.398 ± 0.040	4.86 ± 0.05
Gl 411	M2V	3563 ± 60	-0.38 ± 0.08	0.389 ± 0.013	0.386 ± 0.039	4.84 ± 0.05
Gl 752A	M3V	3558 ± 60	0.10 ± 0.08	0.474 ± 0.016	0.475 ± 0.047	4.76 ± 0.05
Gl 849	M3.5V	3530 ± 60	0.37 ± 0.08	0.470 ± 0.018	0.482 ± 0.048	4.78 ± 0.06
Gl 436	M3V	3479 ± 60	0.01 ± 0.08	0.449 ± 0.019	0.445 ± 0.044	4.78 ± 0.06
Gl 725A	M3V	3441 ± 60	-0.23 ± 0.08	0.351 ± 0.013	0.334 ± 0.033	4.87 ± 0.05
Gl 725B	M3.5V	3345 ± 60	-0.30 ± 0.08	0.273 ± 0.011	0.248 ± 0.025	4.96 ± 0.06
Gl 699	M4V	3228 ± 60	-0.40 ± 0.08	0.186 ± 0.007	0.155 ± 0.015	5.09 ± 0.05
Gl 15B	M3.5V	3218 ± 60	-0.30 ± 0.08	0.192 ± 0.008	0.159 ± 0.016	5.07 ± 0.06
Gl 905	M5.0V	2930 ± 60	0.23 ± 0.08	0.189 ± 0.008	0.145 ± 0.015	5.04 ± 0.06

Table 3. Same as Table 2 for 16 additional stars included in both M15 and this study.

Star	Spectral type	T_{eff}	[M/H]	Radius	Mass	$\log g$
Gl 205	M1.5V	3801 ± 60	0.49 ± 0.08	0.581 ± 0.019	0.633 ± 0.063	4.71 ± 0.05
Gl 514	M1.0V	3727 ± 60	-0.09 ± 0.08	0.483 ± 0.016	0.527 ± 0.053	4.79 ± 0.05
Gl 382	M2V	3623 ± 60	0.13 ± 0.08	0.522 ± 0.019	0.525 ± 0.053	4.72 ± 0.05
Gl 412A	M1.0V	3619 ± 60	-0.37 ± 0.08	0.383 ± 0.013	0.390 ± 0.039	4.86 ± 0.05
Gl 480	M3.5V	3463 ± 60	0.26 ± 0.08	0.466 ± 0.025	0.467 ± 0.047	4.77 ± 0.06
Gl 251	M3V	3448 ± 60	-0.02 ± 0.08	0.358 ± 0.013	0.352 ± 0.035	4.88 ± 0.05
Gl 687	M3.0V	3439 ± 60	0.050 ± 0.080	0.414 ± 0.015	0.405 ± 0.041	4.81 ± 0.05
Gl 581	M3V	3395 ± 60	-0.150 ± 0.080	0.311 ± 0.012	0.292 ± 0.029	4.92 ± 0.06
PM J09553–2715	M3V	3346 ± 60	0.01 ± 0.080	0.321 ± 0.016	0.299 ± 0.030	4.90 ± 0.06
GJ 3378	M4.0V	3340 ± 60	-0.09 ± 0.08	0.269 ± 0.011	0.245 ± 0.024	4.97 ± 0.06
GJ 4333	M3.5V	3324 ± 60	0.24 ± 0.08	0.416 ± 0.020	0.391 ± 0.039	4.79 ± 0.06
GJ 1148	M4.0V	3304 ± 61	0.07 ± 0.08	0.376 ± 0.018	0.336 ± 0.034	4.81 ± 0.06
Gl 876	M3.5V	3247 ± 60	0.17 ± 0.08	0.363 ± 0.014	0.328 ± 0.033	4.83 ± 0.06
Gl 447	M4V	3192 ± 60	-0.020 ± 0.080	0.197 ± 0.008	0.168 ± 0.017	5.08 ± 0.06
GJ 1289	M4.5V	3173 ± 60	0.05 ± 0.08	0.238 ± 0.013	0.202 ± 0.020	4.99 ± 0.06
GJ 1151	M4.5V	3118 ± 60	0.03 ± 0.08	0.190 ± 0.009	0.154 ± 0.015	5.07 ± 0.06

various BERV (with typical maximum difference between observations ranging from 10 to 30 km s⁻¹) allows one to minimize telluric correction errors, and to obtain a template spectrum even in regions where telluric lines are deep enough to render a single observation hardly usable over the corresponding range. All telluric-corrected spectra recorded with an SNR per 2 km s⁻¹ pixel in the *H* band exceeding 50 are used to build the stellar templates. The typical SNR per pixel of these template spectra reaches up to 2000.

3 DERIVING FUNDAMENTAL STELLAR PARAMETERS FROM SPIROU TEMPLATE SPECTRA

In C22, we described and tested a method for determining atmospheric parameters from SPIROU template spectra. We discussed the use of two different models, PHOENIX-ACES (Husser et al. 2013) and MARCS, the differences in the synthetic spectra computed with both models, and their impact on the results. In this work, we update the method to improve the framework and produce more reliable results. Some of these improvements include the implementation of a new continuum normalization procedure and an empirical revision of line parameters for some of the atomic lines used (see Section 3.3). We then further improve the method to retrieve the alpha enhancement ($[\alpha/\text{Fe}]$) as an additional free parameter of our model (see Section 4). We concentrate our efforts on MARCS model

Table 4. Parameter range covered by the computed grid of MARCS synthetic spectra. The range and initial step size are listed along with the level to which the grid is interpolated to reach the final step size.

Variable	Range (and step size)	Interp. factor (and final step size)
T_{eff} (K)	3000–4000 (100)	20 (5)
$\log g$ (dex)	3.5–5.5 (0.5)	50 (0.01)
[M/H] (dex)	-1.5–+1.0 (0.25)	25 (0.01)
$[\alpha/\text{Fe}]$ (dex)	-0.25–+0.5 (0.25)	25 (0.01)

atmospheres, readily available for different values of $[\alpha/\text{Fe}]$ and computed with up-to-date line lists.¹

3.1 The grid of synthetic spectra

We use a grid of synthetic spectra computed from MARCS model atmospheres with Turbospectrum for several T_{eff} , $\log g$, and [M/H] values. This grid is the same as that used in C22, augmented with models computed for $[\alpha/\text{Fe}]$ values ranging from -0.25 to 0.50 dex in steps of 0.25 dex (see Table 4). Spectra were computed for all

¹The grid of PHOENIX-ACES synthetic spectra was not published with multiple $[\alpha/\text{Fe}]$ values for $T_{\text{eff}} > 3500$ K, and updating the line list is not an easy task, hence why we focused on MARCS models in this new study.

available $\log g$, although values below 4.5 dex are not expected to be used in the case of main sequence (Baraffe et al. 2015).

3.2 Stellar analysis procedure

The parameter determination procedure used in this paper is similar to that described in C22. In this section, we briefly summarize the main steps of this process.

3.2.1 Comparison of models to observation templates

SPIRou template spectra are compared to synthetic spectra in order to identify the best-fitting model. Prior to this comparison, the synthetic spectra are binned on the wavelength grid of the SPIRou template. This binning operation is performed through a cubic interpolation and convolution with a rectangular function of width 2 km s^{-1} (representing pixels). The synthetic spectra are also convolved with a Gaussian profile of full width at half-maximum (FWHM) of 4.3 km s^{-1} to account for instrumental broadening (resolving power 70 000). We finally consider the effect of both rotation and macroturbulence on stellar spectra, which we approximate as a Gaussian broadening of FWHM $v_b = 3 \text{ km s}^{-1}$ as in C22. We then extract 400-bin windows around selected lines and adjust the local continuum of the synthetic spectra to match that of the observation template spectrum. This step is particularly challenging in the NIR spectra of M dwarfs, where the large density of atomic and molecular lines renders the pseudo continuum hard to locate. The comparison of synthetic spectra and observation templates is performed on a total of ~ 70 lines, found to be more or less adequately reproduced in synthetic spectra, and sensitive to the atmospheric parameters of interest.

3.2.2 χ^2 minimization

Synthetic spectra for a given range of T_{eff} , $\log g$, $[M/H]$, and $[\alpha/Fe]$ are compared to the SPIRou template for a given star of our sample, yielding a 4D grid of χ^2 values. Given the rough step size of this initial grid (see Section 3.1), we interpolate the synthetic spectra to reach steps of 5 K in T_{eff} and 0.01 dex in $\log g$ and $[M/H]$ around the grid minimum in order to locate the grid minimum and determine the curvature at this position as accurately as possible. A new 4D χ^2 landscape is computed, and a 4D second-degree polynomial is fitted on the 3000 points with smallest χ^2 values.

3.2.3 Error estimation

To estimate error bars on the retrieved parameters, we measure the curvature of the fitted paraboloid. More specifically, we search for the ellipsoid where the χ^2 increases by 1 from the minimum, and project it on each parameter axis. The projected intervals should contain 68.3 per cent of normally distributed data (Press et al. 1992), which we refer to as formal error bars. In C22, we observed that the choice of model has a significant impact on the results, introducing systematics that are not accounted for by our formal error bars computation. To take this effect into account, C22 introduced a second error bar, derived from the root mean square (RMS) difference between the parameters retrieved with both sets of atmospheric models.

In this work, we consider a single model and thus cannot perform a similar operation. We therefore rely on the results of C22 to increase our error bars, by quadratically adding 30 K, 0.05 dex,

and 0.1 dex to the computed formal error bars on T_{eff} , $\log g$, and $[M/H]$, respectively, and refer to these as empirical error bars.

Since we have no means to retrieve an empirical error bar for $[\alpha/Fe]$, we estimate it from those derived on $[M/H]$. We typically compute smaller formal error bars on $[\alpha/Fe]$ than on $[M/H]$, with average values of about 0.015 and 0.005 dex, respectively. The median of the ratio between our formal error bars on $[M/H]$ and on $[\alpha/Fe]$ is of 2.5. To account for some of the systematics and provide a conservative estimate of the error bars on $[\alpha/Fe]$, we choose to quadratically add 0.04 dex to our formal error bars for this parameter. This is consistent with the dispersion of the retrieved $[\alpha/Fe]$ values for stars having $[M/H] > -0.1$ dex, for which thin and thick disc populations blend together.

3.3 Adjustment of the continuum

In this paper, we also revised our continuum adjustment procedure. We extract 400-bin windows around all selected lines for both the SPIRou template and the synthetic spectrum. In each window, we exclude all points of the SPIRou template that fall above the 98th percentile, and may correspond to the poorly corrected telluric emission lines. We then subdivide the 400-bin windows into 40-bin windows, in which we consider all points above the 90th percentile as tracing the continuum. We then fit a straight line through these points to retrieve two continua, one for the template spectrum and one for the synthetic spectrum, which are then used to bring the continua of the template and model spectra to the same level. This procedure sets in the local continuum of both the template and the synthetic spectrum to unity.

4 THE IMPACT OF $[\alpha/Fe]$ ON THE RECOVERED FUNDAMENTAL PARAMETERS

Several studies (Passegger et al. 2019; Schweitzer et al. 2019) assume that the abundances of elements with respect to those of the Sun all differ by the same amount, and typically report values of $[M/H]$ where $[X/H] = [M/H]$ for all elements X with atomic numbers ≥ 3 . This assumption simplifies the modelling but likely affects the estimation of the other parameters. In particular, the abundance of alpha elements (O, Ne, Mg, Si, S, Ar, Ca, and Ti) was shown to depend on the considered stellar population (Fuhrmann 1998; Adibekyan et al. 2013), and models were modified to incorporate an alpha-enhancement parameter ($[\alpha/Fe]$, Gustafsson et al. 2008; Allard, Homeier & Freytag 2011; Husser et al. 2013). In the rest of the paper, $[M/H]$ is used to designate the overall metallicity of all elements but the alpha elements, whose abundances are set to $[\alpha/H] = [M/H] + [\alpha/Fe]$.

The effect of $[\alpha/Fe]$ is visible across the entire SPIRou domain where molecular lines are numerous, and where variations in the abundances of alpha elements, in particular oxygen, leads to significant changes of the model atmospheres.

4.1 $[\alpha/Fe]$ – $[M/H]$ relations

Previous publications analysing M dwarfs analysis adopted a unique $[\alpha/Fe]$ – $[M/H]$ relations for their analysis (Rajpurohit et al. 2018; Marfil et al. 2021). These assume that $[\alpha/Fe] = -0.4[Fe/H]$ for $-1 \leq [Fe/H] < 0$, $[\alpha/Fe] = 0$ for $[Fe/H] \geq 0$, and $[\alpha/Fe] = -1$ for $[Fe/H] < -1$. This relation was also used for the PHOENIX BT-Settl grid of synthetic spectra (Allard et al. 2011).

Due to ongoing spectroscopic large surveys, such relations can nowadays be refined more empirically. For example, this relation

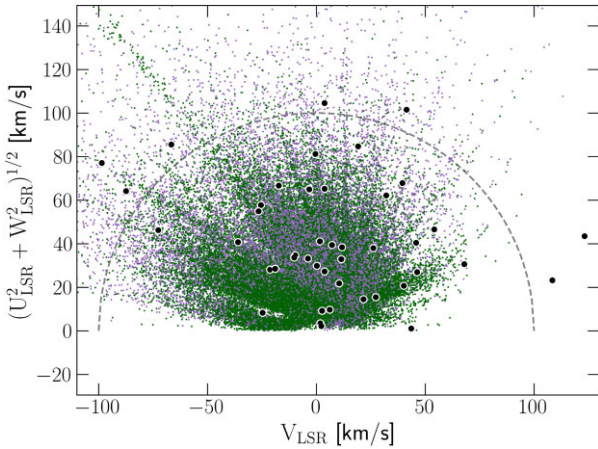


Figure 1. Toomre diagram for the giant stars studied with APOGEE. U, V, and W are the velocities in the Galactic coordinate system, corrected for solar motion (LSR). The purple and green pixels show stars from the thick and thin disc, respectively, distinguished from their elemental abundances. The grey dashed line marks a fiducial boundary at 100 km s^{-1} . The stars studied in this work are marked with a black dot. An alternative figure with labels identifying the stars is presented in Fig. A1.

can be derived by looking at abundances in giants ($4000 \text{ K} < T_{\text{eff}} < 5000 \text{ K}$ and $\log g < 3.5 \text{ dex}$) estimated from the APOGEE survey (Jönsson et al. 2020). These stars can be split into two groups corresponding to two Galactic populations, with the ones from the thick Galactic disc having typically larger $[\alpha/\text{Fe}]$ values than those from the thin Galactic disc. This suggests that distinct $[\alpha/\text{Fe}]$ – $[\text{M}/\text{H}]$ relations should be considered for thin and thick disc stars. It is however still unclear whether these relations also apply to M dwarfs, due to the lack of accurate data for these stars. In this work, we place a fiducial boundary between the low- $[\alpha/\text{Fe}]$ and high- $[\alpha/\text{Fe}]$ stars to define the thin and thick disc populations, respectively. This simplistic classification aims at providing an a posteriori verification that our derived $[\alpha/\text{Fe}]$ values for the targets in our sample are consistent with the literature, rather than investigating the distribution of the stars across the Galactic populations.

Several studies attempted to estimate individual abundances of elements in M dwarfs spectra, from fits of synthetic spectra (Jahandar et al., in preparation; Souto et al. 2022) or equivalent widths (Ishikawa et al. 2020, 2022). In particular, Souto et al. (2022) derived the element abundances for several targets included in our study (GI 411, GI 15A, GI 725A, GI 725B, and GI 880) and obtained $[\alpha/\text{Fe}]$ – $[\text{M}/\text{H}]$ trends suggesting that $[\alpha/\text{Fe}]$ increases for metal-poor stars, consistent with the relations derived for giant stars from APOGEE data.

4.2 Classification of stellar populations from dynamics

Placing the giants studied with APOGEE on a Toomre diagram, we find that the thick disc stars tend to have higher total velocity than thin disc stars (see Figs 1 and A1), and that most of the stars in our sample are found to feature a peculiar velocity below 100 km s^{-1} . Besides, looking at the proportion of thin and thick disc giants with a given velocity (see Fig. 2) provides an estimate of the probability for a star to belong to either population based on its velocity. In particular, stars with a total velocity above 100 km s^{-1} likely belong to the thick disc with a probability > 70 per cent. Assuming that M dwarfs behave as giant stars in this respect suggests that most of our stars, featuring velocities $< 75 \text{ km s}^{-1}$, are likely to belong to the thin

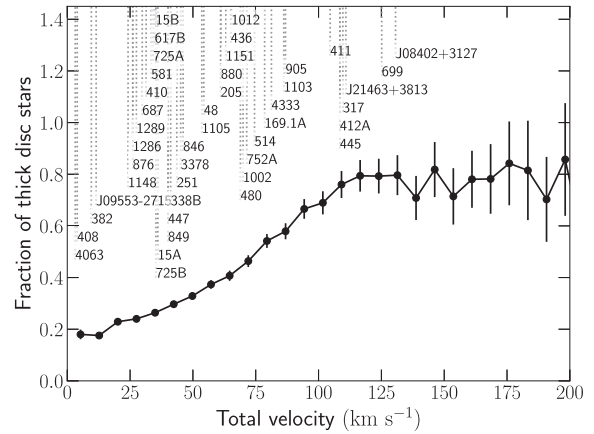


Figure 2. Thick-to-thin disc stars ratio per total velocity bin. The labels mark the velocities of the stars in our sample. This ratio suggests that stars with total velocities $> 100 \text{ km s}^{-1}$ have a probability > 70 per cent to belong to the thick disc.

disc. Only seven of our stars (PM J08402+3127, PM J21463+3813, GI 699, GI 411, GI 317, GI 445, and GI 412A) have a total velocity $> 100 \text{ km s}^{-1}$, and are thus more likely to belong to the thick disc. We come back on this point further in the paper.

Because the choice of $[\alpha/\text{Fe}]$ has a strong impact on the other three parameters, and because we cannot arbitrarily set its value for each star, we chose to fit $[\alpha/\text{Fe}]$ in our analysis procedure.

5 LINE SELECTION AND ADJUSTMENT

The analysis must rely on well-modelled spectral lines in order to provide accurate stellar parameters. Selecting such lines is particularly challenging in the NIR where molecular lines may blend with atomic features, and where models may not accurately reproduce line profiles. SPIRou allows us to select several lines from multiple bands due to its large wavelength coverage. In this work, we revised the line selection performed in C22 and adjusted the properties of some lines, assuming known stellar parameters for three of our calibration stars: GI 699, GI 15A, and GI 411.

5.1 Selecting the stellar lines of interest

Stellar lines are selected by comparing observation templates to synthetic spectra assuming atmospheric parameters as derived from M15, identifying those that are well reproduced by the models, and sensitive to the fundamental parameters we want to constrain. This selection is performed by comparing spectra of calibration stars to model spectra computed for expected parameters. In C22, we selected a set of 26 atomic lines and 40 molecular lines, mainly located in the CO band between 2290 and 2300 nm. In this new study, we added several atomic and OH lines, and rejected some atomic lines that are found to be poorly informative, leading to a new line list containing 17 atomic lines, nine OH lines, and CO lines from the aforementioned (see Table 5). The selected atomic lines are reported in Table 6, and include seven lines from non-alpha elements (Fe, Mn, Al, K, and Na). The table also lists the parameters of the atomic lines, with the hyperfine structure when included in our line lists. These data are used to compute the emergent spectra with the Turbospectrum radiative transfer code.

To exclude some lines, we compared the χ^2 values computed for the expected model (assuming the parameters of M15) and the best

Table 5. Full list of spectral lines used. Lines were identified by depth and wavelength using the VALD data base.

Species	Wavelength (Å)
Ti I	9678.198, 9691.527, 9708.327, 9721.626 22969.597
Fe I	10343.719
Ca I	16201.500
K I	15167.211
Mn I	12979.459
Al I	13126.964, 16723.524, 16755.203
Mg I	15044.357, 15051.818
Na I	22062.420, 22089.692
OH	1672.3418, 1675.3831, 1675.6299
CO	22935.233, 22935.291, 22935.585, 22935.754 22936.343, 22936.627, 22937.511, 22937.900 22939.094, 22939.584, 22941.089, 22941.668 22943.494, 22944.163, 22946.311, 22947.059 22949.544, 22953.195, 22954.059, 22957.263 22958.159, 22961.743, 22962.671, 22966.648 22967.576, 22971.971, 22972.884, 22977.719 22978.596, 22983.888, 22984.707, 22990.488 22991.222, 23112.404, 23124.542, 23150.029, 23163.381

fit obtained (whose parameters may differ from the expected values). Whenever, for our calibration stars, the computed χ^2 is found to be much larger for the expected atmospheric parameters than for those derived with our process, we adjusted the line parameters (see Section 5.2) or excluded the region from our analysis.

5.2 Adjusting line parameters on reference stars

The adjustments were performed on three of our best calibration stars (G1 699, G1 15A, G1 411), by comparing the modelled spectra with various values of the Van Der Waals broadening parameter and oscillator strengths to the SPIRou stellar template spectra. For this step, the parameters published by M15 are assumed for our calibration stars, and $[\alpha/\text{Fe}]$ values were set to 0.2 dex for G1 699 and G1 411 and 0.08 dex for G1 15A, assuming thick and thin disc populations based on velocity.

Significant differences are observed between models and observations, in particular for Ti lines, whose wings appear wider in the models than in observations; this is likely to affect determinations of $\log g$ if not corrected for. Since the wings of these lines are very sensitive to the Van Der Waals collisional broadening parameter, as illustrated on Fig. 3, we decreased the value of this parameter for these lines until a good fit was achieved for all three reference stars, and re-computed a grid of spectra with these adjustments. All corrections applied to the line list are specified in Table 6. Some lines were attributed an Unsöld factor (Unsöld 1955) when no value of the Van der Waals damping parameter (γ_6) was reported in the VALD (Pakhomov, Ryabchikova & Piskunov 2019) line lists.

5.3 Consequence on retrieved parameters

To assess the impact of our adjustments on the retrieved stellar parameters, we perform the analysis on our calibration stars with the new set of synthetic models computed with these adjustments, and derived for each star the four atmospheric parameters of interest with the corresponding error bars. We compare these results to those obtained with the original line list (see Fig. B1). The $[\text{M}/\text{H}]$ and $\log g$ estimates of a few stars are found to be in better agreement with M15. The influence of the correction remains however small on

Table 6. Line list used for the analysis. Columns 1 to 5 present the parameters found in the original list. Modifications to the oscillator strength (Δlggf) and Van der Waals parameter (ΔVdW) are specified in columns 6 and 7, when applicable. When the hyperfine structure (HFS) is available, we display data for all subcomponents. Two distinct prescriptions are found in the Van der Waals column: the commonly reported Van der Waals damping parameter γ_6 is considered if the value is negative; values between 0 and 20 give the value of the fudge factor within the Unsöld approximation.

	Vac. wvl. (Å)	χ_{low}	lggf	VdW	species	Δlggf	ΔVdW
	9678.198	0.84	-0.80	-7.80	Ti I	-	-0.3
	9691.527	0.81	-1.61	-7.80	Ti I	-	-0.2
	9708.327	0.83	-1.01	-7.80	Ti I	-	-0.2
	9721.626	1.50	-1.18	-7.78	Ti I	-0.1	-0.2
	10343.719	2.20	-3.58	-7.80	Fe I	-	-
	10968.389	5.93	-2.16	2.50	Mg I	-	-
	12979.260	2.89	-2.65	2.50	Mn I	-	-
	12979.277	2.89	-2.36	2.50	Mn I	-	-
	12979.295	2.89	-2.62	2.50	Mn I	-	-
	12979.320	2.89	-2.14	2.50	Mn I	-	-
	12979.347	2.89	-2.44	2.50	Mn I	-	-
	12979.364	2.89	-3.39	2.50	Mn I	-	-
	12979.387	2.89	-1.96	2.50	Mn I	-	-
HFS	12979.423	2.89	-2.37	2.50	Mn I	-	-
	12979.450	2.89	-3.31	2.50	Mn I	-	-
	12979.478	2.89	-1.80	2.50	Mn I	-	-
	12979.524	2.89	-2.40	2.50	Mn I	-	-
	12979.560	2.89	-3.44	2.50	Mn I	-	-
	12979.592	2.89	-1.66	2.50	Mn I	-	-
	12979.647	2.89	-2.58	2.50	Mn I	-	-
	12979.692	2.89	-3.79	2.50	Mn I	-	-
	13126.957	3.14	-0.62	2.50	Al I	-	-
	13126.962	3.14	-0.52	2.50	Al I	-	-
	13126.965	3.14	-0.63	2.50	Al I	-	-
HFS	13127.024	3.14	-0.16	2.50	Al I	-	-
	13127.030	3.14	-0.52	2.50	Al I	-	-
	13127.035	3.14	-1.06	2.50	Al I	-	-
	15044.357	5.11	0.12	-7.20	Mg I	-	-
	15051.818	5.11	-0.40	-7.19	Mg I	-	-
	15167.211	2.67	0.63	-6.82	K I	-	-
	16201.500	4.54	0.09	-6.59	Ca I	-	-
	16723.478	4.08	-0.66	-7.15	Al I	-	-
	16723.492	4.08	-0.55	-7.15	Al I	-	-
	16723.510	4.08	-1.09	-7.15	Al I	-	-
	16723.512	4.08	-0.65	-7.15	Al I	-	-
	16723.530	4.08	-0.55	-7.15	Al I	-	-
	16723.557	4.08	-0.19	-7.15	Al I	-	-
	16755.031	4.09	-0.02	-7.22	Al I	-	-
	16755.115	4.09	-0.23	-7.22	Al I	-	-
	16755.126	4.09	-0.71	-7.22	Al I	-	-
	16755.183	4.09	-0.51	-7.22	Al I	-	-
	16755.192	4.09	-0.56	-7.22	Al I	-	-
	16755.203	4.09	-1.66	-7.22	Al I	-	-
	16755.236	4.09	-0.92	-7.22	Al I	-	-
	16755.241	4.09	-0.58	-7.22	Al I	-	-
	16755.249	4.09	-1.28	-7.22	Al I	-	-
	16755.274	4.09	-0.74	-7.22	Al I	-	-
	16755.279	4.09	-1.11	-7.22	Al I	-	-
	16755.293	4.09	-1.06	-7.22	Al I	-	-
	22062.379	3.19	-0.52	2.00	Na I	-	-
	22062.381	3.19	-0.52	2.00	Na I	-	-
	22062.381	3.19	-0.92	2.00	Na I	-	-
	22062.442	3.19	-0.07	2.00	Na I	-	-
	22062.446	3.19	-0.52	2.00	Na I	-	-
	22062.448	3.19	-1.22	2.00	Na I	-	-
	22089.645	3.19	-0.52	2.00	Na I	-	-
HFS	22089.655	3.19	-1.22	2.00	Na I	-	-
	22089.712	3.19	-0.52	2.00	Na I	-	-
	22089.721	3.19	-0.52	2.00	Na I	-	-
	22969.597	1.89	-1.53	-7.79	Ti I	-	-

the retrieved T_{eff} , $\log g$, and $[\text{M}/\text{H}]$ for most stars. Similarly, we look at the effect of the correction on our estimated $[\alpha/\text{Fe}]$ (see Fig. B2), and retrieve values closer to those expected from empirical relations for a few stars, such as G1 849, G1 880, or G1 905.

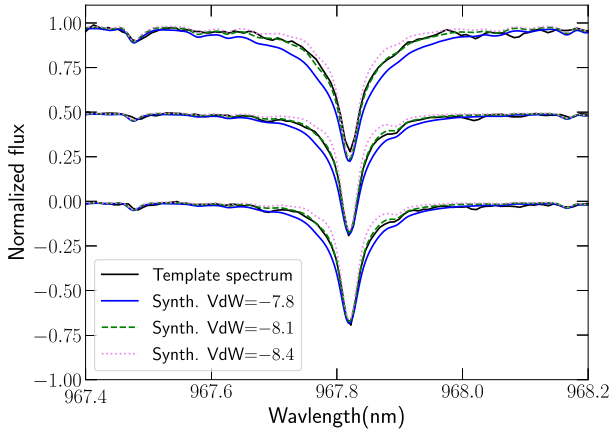


Figure 3. Example of Ti line. The black lines present the template spectra of three stars, from top to bottom: G1 699, G1 15A, and G1 411. Synthetic spectra with three different values of Van der Waals damping parameter are plotted for each star. The initial value found in the list was -7.8 , and we adopt a value -8.1 for our analysis.

We also perform a comparison between the results obtained while fitting $[\alpha/\text{Fe}]$ or if the parameter is set to 0 (see Fig. B3). We find that fitting $[\alpha/\text{Fe}]$ allows us to significantly reduce the scatter on the retrieved $\log g$, and to obtain $[\text{M}/\text{H}]$ estimates in better agreement with our reference study, with the exception of G1 905, for which $[\text{M}/\text{H}]$ is found about 0.2 dex smaller than that reported by M15, who relied on empirically calibrated relations between equivalent widths of some atomic features and metallicity. Subsequent tests showed that a variation of $[\alpha/\text{Fe}]$ of 0.05 dex can lead to a 0.2 dex variation on $[\text{M}/\text{H}]$ for this star.

Two binaries are included in our study: G1 725 and G1 15. For both systems, we retrieve $[\text{M}/\text{H}]$ for each component that are in good agreement, with differences of 0.02 dex for G1 725 and 0.09 dex for G1 15, thereby improving over our initial study where this difference reached 0.21 dex in the case of G1 15A (C22). For G1 15, we also observe a small difference in the $[\alpha/\text{Fe}]$ values of 0.06 dex, again consistent with the estimated empirical error bars.

6 RESULTS

We performed the analysis described in Section 3 with the updated list presented in Section 5, on our 44 selected targets (see Section 2.1). Figs 4 and A2 present a comparison between the results and the parameters published by M15 for the 28 stars common to both samples. Fig. C1 (available as supplementary material) presents the best fit obtained on all lines for five stars in our sample. The retrieved T_{eff} , $\log g$, $[\text{M}/\text{H}]$, and $[\alpha/\text{Fe}]$ are listed in Table 7 along with an estimate of the stellar masses and radii.

6.1 Effective temperature

For the 28 stars also studied by M15, we compare our results to the reported effective temperatures (Fig. 4). The overall retrieved T_{eff} are in good agreement with M15 with an RMS on the residuals of the order of 45 K, compatible with the error bars reported by M15. We observe a tendency to derive higher T_{eff} for cooler stars, with a deviation of up to 140 K for G1 905. This trend may reflect discrepancies in the physics used in the MARCS models at the lowest side of their temperature range, or alternatively probe systematics in M15. To assess the internal dispersion of our results, we fit a line

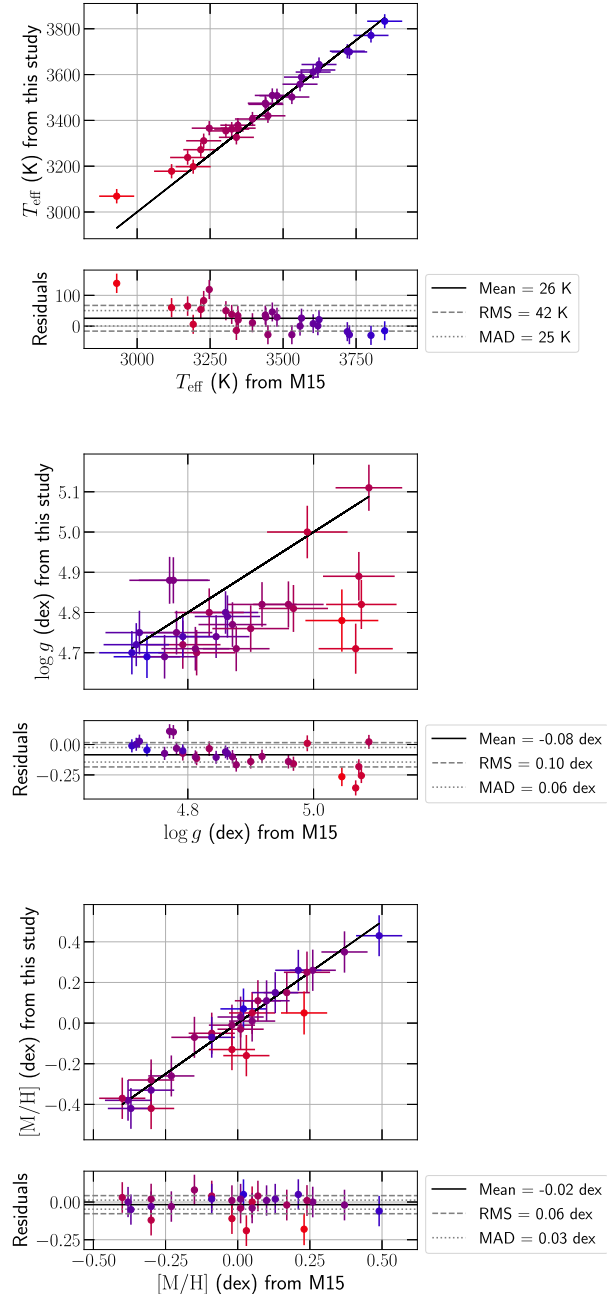


Figure 4. Comparison between retrieved parameters and value published by M15 for 23 stars common to both samples. The temperature is colour coded from red (coolest) to blue (hottest). An alternative figure with labels identifying the stars is presented in Fig. A2.

through our retrieved results (of slope 0.85 ± 0.02). For these 28 stars, the RMS about the trend in T_{eff} is of about 25 K, of the order of our estimated error bars.

Fig. D1 presents a similar comparison to the parameters retrieved by Passegger et al. (2019), who performed fits of PHOENIX-ACES synthetic spectra on high-resolution CARMENES data. The RMS on the residuals is then of about 60 K, again, of the order of the typically published error bars. We point out that Passegger et al. (2019), as well as other references such as Marfil et al. (2021), also find higher T_{eff} values than M15 for the coolest star of our sample.

Table 7. Retrieved parameters of the star in our sample. Columns 2 to 5 present the stellar parameters estimated from our fitting procedure. Columns 6 through 9, respectively, present the *GaiA* G -, J -, and K -band absolute magnitudes and parallaxes extracted from SIMBAD. Column 10 lists the log of the logarithmic bolometric luminosity (with respect to that of the Sun) derived from M_G . Columns 11 and 12 present the radius computed from T_{eff} and M_J and mass derived from M_K -mass relations. Column 13 presents alternative log g estimates computed from columns 11 and 12.

Star	T_{eff}	log g	[M/H]	[α /Fe]	M_G	M_J	M_K	Parallax	$\log(L_*/L_\odot)$	Radius	Mass	alt. log g
Gl 338B	3952 ± 30	4.71 ± 0.05	-0.08 ± 0.10	0.05 ± 0.04	8.046 ± 0.003	5.77 ± 0.17	5.13 ± 0.02	157.88 ± 0.02	-1.090 ± 0.011	0.609 ± 0.012	0.58 ± 0.02	4.63 ± 0.02
Gl 410	3842 ± 31	4.87 ± 0.05	0.05 ± 0.10	0.05 ± 0.04	8.426 ± 0.003	6.14 ± 0.02	5.30 ± 0.02	83.76 ± 0.02	-1.239 ± 0.002	0.543 ± 0.009	0.55 ± 0.02	4.71 ± 0.02
Gl 846	3833 ± 31	4.69 ± 0.05	0.07 ± 0.10	-0.01 ± 0.04	8.282 ± 0.003	6.07 ± 0.02	5.20 ± 0.02	94.56 ± 0.05	-1.204 ± 0.002	0.568 ± 0.009	0.57 ± 0.02	4.68 ± 0.02
Gl 205	3771 ± 31	4.70 ± 0.05	0.43 ± 0.10	-0.08 ± 0.04	8.327 ± 0.003	6.05 ± 0.06	5.12 ± 0.06	175.31 ± 0.02	-1.202 ± 0.004	0.588 ± 0.010	0.58 ± 0.02	4.66 ± 0.02
Gl 880	3702 ± 31	4.72 ± 0.05	0.26 ± 0.10	-0.04 ± 0.04	8.611 ± 0.003	6.18 ± 0.02	5.34 ± 0.02	145.62 ± 0.03	-1.272 ± 0.001	0.563 ± 0.009	0.55 ± 0.02	4.67 ± 0.02
Gl 514	3699 ± 31	4.74 ± 0.05	-0.07 ± 0.10	0.04 ± 0.04	8.793 ± 0.003	6.49 ± 0.02	5.62 ± 0.03	131.10 ± 0.03	-1.382 ± 0.001	0.497 ± 0.008	0.50 ± 0.02	4.74 ± 0.02
Gl 382	3644 ± 31	4.75 ± 0.05	0.15 ± 0.10	-0.02 ± 0.04	8.897 ± 0.003	6.45 ± 0.02	5.58 ± 0.02	129.75 ± 0.03	-1.384 ± 0.001	0.511 ± 0.009	0.51 ± 0.02	4.73 ± 0.02
Gl 412A	3620 ± 31	4.79 ± 0.05	-0.42 ± 0.10	0.12 ± 0.04	9.460 ± 0.003	7.08 ± 0.02	6.32 ± 0.02	203.89 ± 0.03	-1.628 ± 0.001	0.391 ± 0.007	0.39 ± 0.02	4.84 ± 0.03
Gl 15A	3611 ± 31	4.80 ± 0.05	-0.33 ± 0.10	0.10 ± 0.04	9.460 ± 0.003	7.49 ± 0.26	6.26 ± 0.02	280.71 ± 0.02	-1.740 ± 0.034	0.345 ± 0.015	0.39 ± 0.02	4.96 ± 0.04
Gl 411	3589 ± 31	4.74 ± 0.05	-0.38 ± 0.10	0.19 ± 0.04	9.522 ± 0.003	7.17 ± 0.24	6.31 ± 0.05	392.75 ± 0.03	-1.659 ± 0.010	0.383 ± 0.008	0.39 ± 0.02	4.86 ± 0.03
Gl 752A	3558 ± 31	4.69 ± 0.05	0.11 ± 0.10	-0.01 ± 0.04	9.240 ± 0.003	6.72 ± 0.03	5.81 ± 0.02	169.06 ± 0.02	-1.500 ± 0.001	0.469 ± 0.008	0.47 ± 0.02	4.77 ± 0.02
Gl 48	3529 ± 31	4.68 ± 0.05	0.08 ± 0.10	0.07 ± 0.04	9.364 ± 0.003	6.72 ± 0.03	5.87 ± 0.02	121.46 ± 0.02	-1.514 ± 0.002	0.469 ± 0.008	0.46 ± 0.02	4.76 ± 0.03
Gl 617B	3525 ± 31	4.84 ± 0.06	0.20 ± 0.10	0.00 ± 0.04	9.459 ± 0.003	6.75 ± 0.02	5.91 ± 0.02	92.90 ± 0.02	-1.532 ± 0.002	0.460 ± 0.008	0.45 ± 0.02	4.77 ± 0.03
Gl 480	3509 ± 31	4.88 ± 0.06	0.26 ± 0.10	-0.01 ± 0.04	9.565 ± 0.003	6.81 ± 0.02	5.92 ± 0.02	70.11 ± 0.03	-1.562 ± 0.002	0.449 ± 0.008	0.45 ± 0.02	4.79 ± 0.03
Gl 436	3508 ± 31	4.75 ± 0.05	0.03 ± 0.10	0.00 ± 0.04	9.631 ± 0.003	6.95 ± 0.02	6.12 ± 0.02	102.30 ± 0.03	-1.609 ± 0.002	0.425 ± 0.008	0.42 ± 0.02	4.80 ± 0.03
Gl 849	3502 ± 31	4.88 ± 0.06	0.35 ± 0.10	-0.04 ± 0.04	9.511 ± 0.003	6.78 ± 0.02	5.87 ± 0.02	113.44 ± 0.03	-1.548 ± 0.002	0.458 ± 0.008	0.46 ± 0.02	4.78 ± 0.03
Gl 408	3487 ± 31	4.79 ± 0.05	-0.09 ± 0.10	0.04 ± 0.04	9.831 ± 0.003	7.17 ± 0.02	6.36 ± 0.01	148.20 ± 0.03	-1.695 ± 0.002	0.390 ± 0.007	0.38 ± 0.02	4.83 ± 0.03
Gl 687	3475 ± 31	4.71 ± 0.05	0.01 ± 0.10	0.06 ± 0.04	9.739 ± 0.003	7.05 ± 0.02	6.26 ± 0.02	219.79 ± 0.02	-1.649 ± 0.002	0.414 ± 0.007	0.39 ± 0.02	4.80 ± 0.03
Gl 725A	3470 ± 31	4.77 ± 0.06	-0.26 ± 0.10	0.15 ± 0.04	10.120 ± 0.003	7.45 ± 0.02	6.70 ± 0.02	283.84 ± 0.02	-1.809 ± 0.002	0.345 ± 0.006	0.33 ± 0.02	4.88 ± 0.03
Gl 317	3421 ± 31	4.71 ± 0.06	0.23 ± 0.10	-0.04 ± 0.04	9.859 ± 0.003	7.03 ± 0.03	6.12 ± 0.02	65.88 ± 0.04	-1.657 ± 0.004	0.423 ± 0.008	0.42 ± 0.02	4.80 ± 0.03
Gl 251	3420 ± 31	4.71 ± 0.06	-0.01 ± 0.10	-0.01 ± 0.04	10.129 ± 0.003	7.37 ± 0.02	6.54 ± 0.02	179.06 ± 0.03	-1.786 ± 0.003	0.365 ± 0.007	0.35 ± 0.02	4.86 ± 0.03
Gl 4063	3419 ± 31	4.77 ± 0.06	0.42 ± 0.10	-0.07 ± 0.04	9.982 ± 0.003	7.00 ± 0.02	—	91.80 ± 0.02	-1.662 ± 0.004	0.422 ± 0.008	—	—
Gl 581	3406 ± 31	4.82 ± 0.06	-0.07 ± 0.10	0.01 ± 0.04	10.425 ± 0.003	7.71 ± 0.03	6.84 ± 0.02	158.72 ± 0.03	-1.917 ± 0.002	0.317 ± 0.006	0.31 ± 0.02	4.92 ± 0.03
Gl 725B	3379 ± 31	4.82 ± 0.06	-0.28 ± 0.10	0.14 ± 0.04	10.790 ± 0.003	7.99 ± 0.02	7.27 ± 0.02	283.84 ± 0.03	-2.038 ± 0.003	0.280 ± 0.005	0.25 ± 0.02	4.95 ± 0.04
Gl 876	3366 ± 31	4.80 ± 0.06	0.15 ± 0.10	0.04 ± 0.04	10.528 ± 0.003	7.59 ± 0.02	6.66 ± 0.02	214.04 ± 0.04	-1.892 ± 0.004	0.333 ± 0.006	0.33 ± 0.02	4.91 ± 0.03
PM J09553-2715	3366 ± 31	4.76 ± 0.06	-0.03 ± 0.10	-0.02 ± 0.04	10.629 ± 0.003	7.84 ± 0.02	6.96 ± 0.02	91.74 ± 0.04	-1.979 ± 0.003	0.302 ± 0.006	0.29 ± 0.02	4.94 ± 0.04
Gl 1012	3363 ± 31	4.66 ± 0.06	0.07 ± 0.10	0.01 ± 0.04	10.268 ± 0.003	7.40 ± 0.02	6.56 ± 0.02	74.71 ± 0.04	-1.811 ± 0.003	0.367 ± 0.007	0.35 ± 0.02	4.85 ± 0.03
Gl 4333	3362 ± 31	4.72 ± 0.06	0.25 ± 0.10	0.02 ± 0.04	10.233 ± 0.003	7.27 ± 0.03	6.38 ± 0.02	94.37 ± 0.03	-1.767 ± 0.006	0.386 ± 0.008	0.37 ± 0.02	4.84 ± 0.03
Gl 445	3356 ± 31	4.85 ± 0.06	-0.24 ± 0.10	0.14 ± 0.04	10.949 ± 0.003	8.12 ± 0.02	7.35 ± 0.03	190.33 ± 0.02	-2.094 ± 0.003	0.266 ± 0.005	0.24 ± 0.02	4.97 ± 0.04
Gl 1148	3354 ± 31	4.70 ± 0.06	0.11 ± 0.10	0.01 ± 0.04	10.370 ± 0.003	7.40 ± 0.02	6.61 ± 0.02	90.69 ± 0.03	-1.820 ± 0.004	0.365 ± 0.007	0.34 ± 0.02	4.84 ± 0.03
PM J08402 + 3127	3347 ± 31	4.76 ± 0.06	-0.08 ± 0.10	0.01 ± 0.04	10.739 ± 0.003	7.87 ± 0.02	7.05 ± 0.02	89.07 ± 0.03	-1.998 ± 0.003	0.299 ± 0.006	0.28 ± 0.02	4.93 ± 0.04
Gl 3378	3326 ± 31	4.81 ± 0.06	-0.05 ± 0.10	-0.01 ± 0.04	10.975 ± 0.003	8.02 ± 0.02	7.20 ± 0.02	129.30 ± 0.03	-2.068 ± 0.004	0.279 ± 0.005	0.26 ± 0.02	4.96 ± 0.04
Gl 1105	3324 ± 31	4.63 ± 0.07	-0.04 ± 0.10	-0.05 ± 0.04	10.931 ± 0.003	8.00 ± 0.02	7.14 ± 0.03	112.99 ± 0.03	-2.056 ± 0.004	0.283 ± 0.005	0.27 ± 0.02	4.96 ± 0.04
Gl 699	3311 ± 31	5.11 ± 0.06	-0.37 ± 0.10	0.16 ± 0.04	11.884 ± 0.003	8.93 ± 0.02	8.21 ± 0.02	546.98 ± 0.04	-2.432 ± 0.004	0.185 ± 0.004	0.16 ± 0.02	5.11 ± 0.06
Gl 169.1A	3307 ± 31	4.71 ± 0.06	0.13 ± 0.10	-0.07 ± 0.04	10.994 ± 0.003	7.91 ± 0.02	7.01 ± 0.02	181.24 ± 0.05	-2.037 ± 0.005	0.292 ± 0.006	0.28 ± 0.02	4.96 ± 0.04
PM J21463 + 3813	3305 ± 33	5.06 ± 0.08	-0.38 ± 0.10	0.25 ± 0.04	11.591 ± 0.003	8.71 ± 0.02	7.96 ± 0.02	141.89 ± 0.02	-2.335 ± 0.003	0.208 ± 0.004	0.18 ± 0.02	5.06 ± 0.06
Gl 15B	3272 ± 31	4.89 ± 0.06	-0.42 ± 0.10	0.04 ± 0.04	11.928 ± 0.003	9.03 ± 0.02	8.19 ± 0.02	280.69 ± 0.03	-2.465 ± 0.004	0.182 ± 0.004	0.16 ± 0.02	5.13 ± 0.06
Gl 1289	3238 ± 32	5.00 ± 0.07	0.05 ± 0.10	-0.00 ± 0.04	11.556 ± 0.003	8.50 ± 0.03	7.61 ± 0.02	119.58 ± 0.06	-2.269 ± 0.007	0.233 ± 0.005	0.21 ± 0.02	5.03 ± 0.05
Gl 447	3198 ± 31	4.82 ± 0.06	-0.13 ± 0.10	-0.01 ± 0.04	11.960 ± 0.003	8.86 ± 0.02	8.01 ± 0.02	296.31 ± 0.03	-2.419 ± 0.006	0.201 ± 0.004	0.18 ± 0.02	5.08 ± 0.06
Gl 1151	3178 ± 31	4.71 ± 0.06	-0.16 ± 0.10	-0.03 ± 0.04	12.158 ± 0.003	8.96 ± 0.03	8.11 ± 0.02	124.34 ± 0.05	-2.468 ± 0.009	0.193 ± 0.004	0.17 ± 0.02	5.10 ± 0.06
Gl 1103	3170 ± 31	4.67 ± 0.06	-0.03 ± 0.10	-0.00 ± 0.04	11.818 ± 0.003	8.66 ± 0.02	7.83 ± 0.02	107.85 ± 0.04	-2.344 ± 0.007	0.224 ± 0.005	0.19 ± 0.02	5.03 ± 0.05
Gl 905	3069 ± 31	4.78 ± 0.08	0.05 ± 0.11	-0.06 ± 0.04	12.881 ± 0.003	9.39 ± 0.03	8.43 ± 0.02	316.48 ± 0.04	-2.664 ± 0.012	0.165 ± 0.004	0.15 ± 0.02	5.17 ± 0.07
Gl 1002	2980 ± 33	4.70 ± 0.08	-0.33 ± 0.11	-0.00 ± 0.04	13.347 ± 0.003	9.90 ± 0.02	9.01 ± 0.02	206.35 ± 0.05	-2.864 ± 0.009	0.139 ± 0.003	0.12 ± 0.02	5.22 ± 0.09
Gl 1286	2961 ± 33	4.55 ± 0.12	-0.23 ± 0.10	-0.04 ± 0.04	13.344 ± 0.003	9.87 ± 0.02	8.90 ± 0.02	139.34 ± 0.04	-2.855 ± 0.010	0.142 ± 0.004	0.12 ± 0.02	5.21 ± 0.08

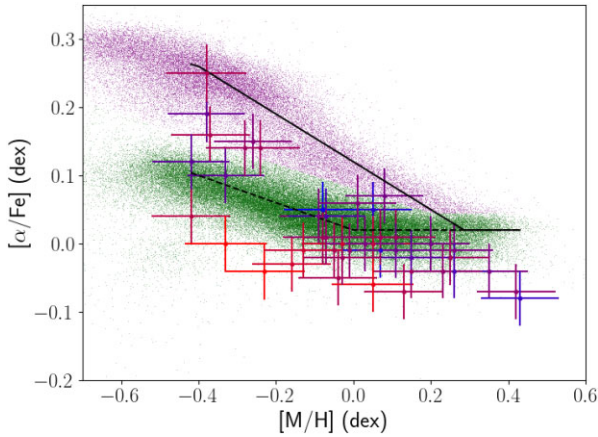


Figure 5. Retrieved $[\alpha/\text{Fe}]$ plotted against $[\text{M}/\text{H}]$ for the 44 targets in our sample. The solid and dashed black lines mark empirical thick and thin disc $[\text{M}/\text{H}]$ – $[\alpha/\text{Fe}]$ relations, respectively. The coloured pixels mark the position of giants studied by APOGEE, with the purple and green colours marking those expected to be from the thick and thin disc, respectively. An alternative figure with labels identifying the stars is presented in Fig. A3.

6.2 Metallicity and alpha-enhancement

For the 28 stars studied in this work and in M15, the $[\text{M}/\text{H}]$ values recovered with our analysis are in good agreement, with an RMS on the residuals of about 0.1 dex, of the order of our estimated empirical error bar for this parameter. Here again, the largest deviation is observed for the coolest stars in our sample, for which we find lower $[\text{M}/\text{H}]$ than M15, but for which other studies (Passegger et al. 2019; Marfil et al. 2021) also find different values than M15 (see Figs D1 and D2).

Comparing our results to the values published by Passegger et al. (2019, Fig. D1), we find a much larger RMS on the residuals of about 0.16 dex. These results illustrate the difficulty to estimate the accuracy of the parameters derived from fits of synthetic spectra which depends on the assumed reference on which to rely.

Fitting $[\alpha/\text{Fe}]$ as an additional dimension in our process allowed us to significantly improve the estimate of $[\text{M}/\text{H}]$ for cool metal-poor stars. Because our line list contains several features sensitive to $[\alpha/\text{Fe}]$ variations, we are able to obtain reliable estimates of this parameter without the need to set priors. Figs 5 and A3 present the retrieved $[\alpha/\text{Fe}]$ as a function of the recovered $[\text{M}/\text{H}]$ for the 44 stars of our sample. These results are globally consistent with the expected trends estimated from the APOGEE data for giants and suggest that most of our stars belong to the thin Galactic disc, with a few exception such as GI 699, GI 411, PM J21463+3813, and GI 445 which would more likely belong to the thick Galactic disc. GI 725 A and B are found at the limit of the fiducial boundary between thick and thin disc, and are therefore difficult to classify.

6.3 Masses and radii

Mann et al. (2019) derived a K -band magnitude (M_K) – mass–metallicity empirical relation. We use this relation to derive the masses of the targets in our sample. Radii for the studied stars can be computed from the recovered T_{eff} and the bolometric luminosity using Stefan–Boltzmann law. Bolometric luminosities are directly computed from 2MASS J - and *Gaia* (DR2) G -band absolute magnitudes (M_J and M_G , respectively) and bolometric corrections (Cifuentes et al. 2020). All magnitudes used in this work

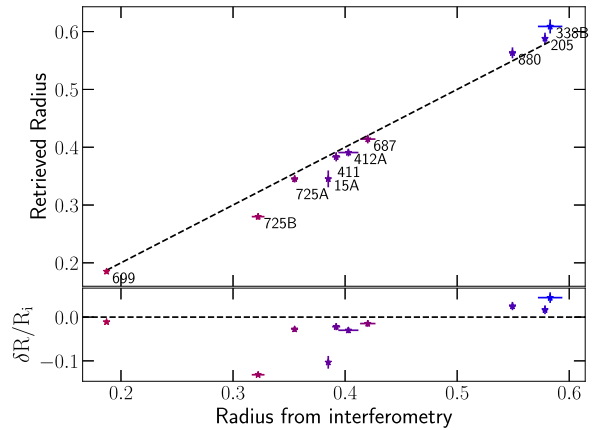


Figure 6. Comparison between radii retrieved from fits and computed from interferometric measurements (Boyajian et al. 2012) for nine stars. The symbol colour depicts the temperature from red (cool) to blue (hot). The larger error bars originate from uncertainties on the M_J measurements published by the 2MASS survey. The bottom plot displays the relative difference between our estimated radii and those computed from interferometric measurements.

were extracted from SIMBAD.² In this work, we chose to derive the luminosities from bolometric corrections and absolute magnitudes rather than to rely on bolometric luminosities reported by authors such as Cifuentes et al. (2020) or M15. This allows us to produce self-consistent results for all the stars in our sample as these studies do not typically report values for all our targets. Several tests allowed to verify that the reported values and those derived from bolometric corrections are in fair agreement for most stars (see Fig. E1). One should note that the 2MASS survey attributes a quality flag to the reported magnitudes, which may not systematically be accounted for by reported uncertainties. We compare our retrieved radii (R_f) to those computed from interferometry (R_i) by Boyajian et al. (2012, see Fig. 6). We find values that are consistent with interferometric measurements for the nine stars studied by Boyajian et al. (2012), with a dispersion on $\delta R/R_i \approx 5$ per cent, with $\delta R = R_f - R_i$.

We note that the radius retrieved from interferometry for GI 725B is significantly larger than the one we estimate with this method; coupled with the measured magnitude, it would yield an effective temperature of $T_{\text{eff}} = 3145 \pm 10$ K, i.e. 200 K cooler than the values derived by most studies (M15, C22 Fouqué et al. 2018; Marfil et al. 2021) and ours. This discrepancy was also observed and reported by M15. The apparent inconsistency in these results calls for an in-depth investigation of GI 725B.

We locate our stars in a Hertzsprung–Russell (HR) diagram (see Figs 7 and A4). We compare our results to the isochrone computed by Baraffe et al. (2015). Our results tend to be in good agreement with the model, with points scattered around the isochrone, which can be attributed to metallicity. Isochrones computed with the Dartmouth stellar evolution program (DSEP, Dotter et al. 2008) for different metallicities confirm the dependency on $[\text{M}/\text{H}]$. We also observe a strong divergence between the DSEP models and those of Baraffe et al. (2015), in particular for stars with masses lower than $0.3 M_{\odot}$.

Our estimated radii and masses are found in good agreement with mass–radius relations expected from stellar evolution models (see Figs 8 and A5, Feiden & Chaboyer 2012). We further note a good agreement between our derived masses and radii and those reported

²<http://simbad.cds.unistra.fr/simbad/>

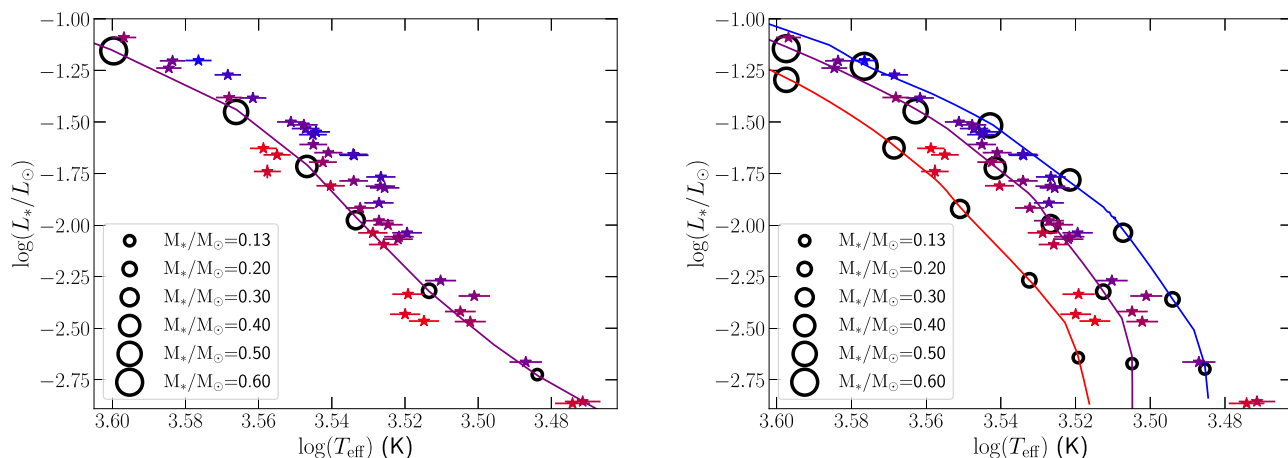


Figure 7. HR diagram showing the position of the stars in our sample. Luminosity was computed from G -band magnitude retrieved through SIMBAD. The metallicity is colour coded from red to blue (low to high metallicity, respectively). On the left-hand panel, the purple solid line presents the isochrone computed by Baraffe et al. (2015) at solar metallicity. On the right-hand panel, the red, purple, and blue solid lines present the DSEP stellar isochrones for $[M/H] = -0.5$ dex, $[M/H] = 0.0$ dex, and $[M/H] = 0.5$ dex, respectively. An age of 5 Gyr is assumed for all isochrones. The black circles mark the position of different stellar masses for each metallicity. An alternative figure with labels identifying the stars is presented in Fig. A4.

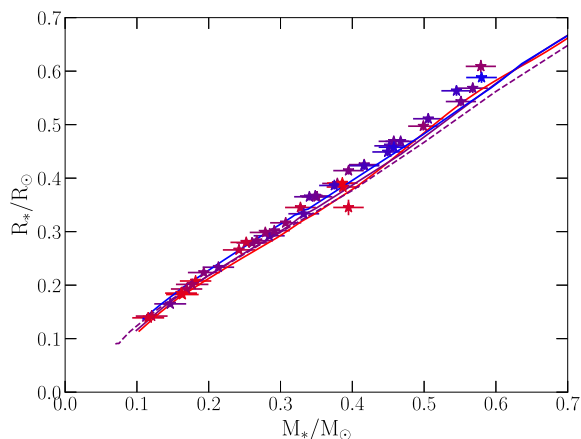


Figure 8. Mass–radius diagram showing the position of the stars in our sample. The metallicity is colour coded from red to blue (low to high metallicity, respectively). The red, purple, and blue solid lines present the mass–radius relation predicted by the DSEP models for $[M/H] = -0.5$ dex, $[M/H] = 0.0$ dex, and $[M/H] = 0.5$ dex, respectively. The purple dashed line presents the mass–radius relationship predicted by the models of Baraffe et al. (2015), at solar metallicity. An age of 5 Gyr is assumed for all models. An alternative figure with labels identifying the stars is presented in Fig. A5.

by M15 (see Fig. F1), with a relative dispersion of 4 per cent on both parameters.

6.4 Surface gravity

Surface gravity is known to be difficult to constrain for M dwarfs. Several studies chose to fix this parameter from semi-empirical relations or evolutionary models (Rajpurohit et al. 2018; Pasegger et al. 2019). Following C22, we fit this parameter. Our new estimates are in better agreement with M15 than those of C22, showing that the various improvements brought to our analysis (see Section 3–5) helped solving the issue.

From the masses and radii derived in Section 6.3 we compute new $\log g$ values, and compare these to the values obtained from the spectral fitting procedure (see Figs 9 and A6). We observe significant

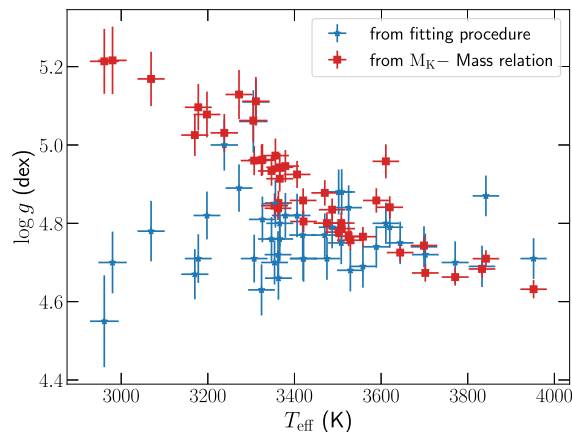


Figure 9. Comparison of the $\log g$ derived from our fitting procedure and those computed from M_K –mass relation. An alternative figure with labels identifying the stars is presented in Fig. A6.

differences between the two sets of $\log g$ values, and compute an RMS on the residuals of about 0.2 dex. This dispersion is also the result of larger discrepancies at low T_{eff} and the RMS value computed when ignoring the six coolest stars in our sample falls to 0.11 dex. This may suggest that, for some yet unclear reason, we underestimate the $\log g$ of the coolest stars with our fitting procedure.

7 DISCUSSION AND CONCLUSIONS

In this work, we improved and extended a method designed to retrieve the atmospheric parameters of M dwarfs from high-resolution spectroscopic observations using state-of-the-art synthetic spectra computed with Turbospectrum from MARCS model atmospheres. Our analysis consists in comparing these models to high-SNR template spectra built from tens to hundreds of observations collected with SPIRou. We extend the work initiated in C22 and applied our new tool to our SLS sample of 44 M dwarfs.

Recent publications (Rajpurohit et al. 2018; Marfil et al. 2021) included empirical $[\alpha/\text{Fe}]$ – $[M/H]$ relations in their analysis, or relied on models that did so, in order to constrain T_{eff} or $[M/H]$. In this

work, the fitting procedure, initially developed to constrain T_{eff} , $\log g$, and $[M/H]$, was extended to also include a fit of $[\alpha/Fe]$, motivated by the large impact this parameter has on the derivation of the other stellar parameters. We retrieve $[\alpha/Fe]$ values that are consistent with empirical trends observed when studying giants (Adibekyan et al. 2013). We find that the coolest low-metallicity stars in our sample are the most sensitive to $[\alpha/Fe]$. This is likely due to the presence of strong O-bearing molecular bands (e.g. CO) in the NIR spectra at low T_{eff} , strongly impacted by variations in the abundances of alpha elements, in particular oxygen.

In this paper, we revised the line list used in C22, and updated the continuum adjustment procedure to improve the fit quality. This updated list contains 17 atomic lines, nine OH lines, and about 40 molecular lines found in the CO band redward of 2293 nm, which represents a very small subset of the lines that are included in the models and those present in the observed template spectra (which in most cases do not match well). Previous studies have attempted to refine the parameters of some atomic lines for their analysis (Petit et al. 2021). Here, we tried to improve the fits of synthetic spectra to SPIRou templates by adjusting the values of Van Der Waals broadening parameters and oscillator strengths for a few of the selected lines. We assumed the parameters published by M15 for three calibration stars (GI 699, GI 15A, and GI 411) to perform this step. These corrections, and in particular those applied to the Van Der Waals parameter of Ti lines, helped to bring our $\log g$ estimates closer to those of M15 for some targets. One should note that these corrections may not be the sole result of uncertainties in the line parameters, and may also reflect inaccuracies of the atmospheric models.

With the implemented improvements and updated line list, we recover parameters in good agreement with M15 for 28 stars included in both studies. We retrieve T_{eff} with a typical dispersion of about 45 K, lower than the uncertainties reported by M15, although larger than our estimated error bars of about 30 K. This difference is also the result of a trend observed in the retrieved T_{eff} values, as we tend to derive larger T_{eff} for cool stars than M15. The dispersion about this trend is of the order of 25 K, of the order of our empirical error bars. We also obtain $[M/H]$ values with a dispersion of 0.06 dex, consistent with our error bars estimated to about 0.1 dex. Finally, $\log g$ is in better agreement with M15 compared to the values reported in C22, although we tend to recover smaller estimates than M15 for the coolest stars in our sample.

For our 44 targets, we extracted *Gaia* G -, J -, and K -band magnitudes from SIMBAD, along with parallaxes, when available. We computed the radii for our sample from T_{eff} , absolute J -band magnitude (M_J), and bolometric corrections (Cifuentes et al. 2020). Interferometric data published by Boyajian et al. (2012) for nine of these stars reported angular diameters that are consistent with our retrieved radii, with a relative dispersion of about 5 per cent. Additionally, we derive the masses of the stars in our sample from M_K -mass relations (Mann et al. 2019). Our derived masses and radii tend to be in good agreement with mass-radius relationships predicted by evolutionary models. We note a slight tendency to estimate larger radii than those predicted by the DSEP models and those of Baraffe et al. (2015). This tendency was reported in the literature (Feiden & Chaboyer 2013; Jackson, Deliyannis & Jeffries 2018) and different hypotheses were proposed, attributing the phenomenon to metallicity, modelling assumptions, or radius inflation induced by the presence of magnetic fields. From our masses and radii estimates, we compute new $\log g$ values, and compare them to those derived from the fitting procedure. We find significant discrepancies between the two sets of $\log g$ values, especially at the lowest temperatures. This difference suggests that we tend to

underestimate $\log g$ for the coolest stars in our sample with our fitting procedure. Fixing $\log g$ to higher values for the coolest stars in our sample results in an increase in T_{eff} of 20–50 K, an increase in $[M/H]$ of up to 0.2 dex, and slight increases in $[\alpha/Fe]$ by less than 0.04 dex. This may reflect MARCS models being less accurate at temperatures close to 3000 K, i.e. close to the lower limit of our model temperature grid.

We also retrieved $[\alpha/Fe]$ values for the 44 stars in our sample, but lack references for most of these targets. Given that T_{eff} , $\log g$, and $[M/H]$ are very sensitive to small variations in $[\alpha/Fe]$, the latter should be carefully considered when fitting models to spectra of M dwarfs. To assess the quality of the constraint on this parameter, we place our stars in a $[\alpha/Fe]$ - $[M/H]$ plane, and find that the recovered $[\alpha/Fe]$ are in good agreement with values expected from empirical relations. We find that a few stars, in particular GI 699, GI 445, PM J21463+3813, and GI 411, have relatively large retrieved $[\alpha/Fe]$ values and are likely to belong to the thick Galactic disc, while most of our stars are likely to belong to thin disc, with lower $[\alpha/Fe]$ values. These results are somewhat consistent with the computed velocities, larger than 100 km s⁻¹ for these four stars. Although GI 317 and PM J09553-2715 also feature high velocities, their supersolar metallicities make it difficult to reliably conclude about the disc population these stars belong to. GI 412A also has a velocity above 100 km s⁻¹, but we derive an $[\alpha/Fe]$ value smaller than that expected for the thick disc. These results are compatible with previous classification of these stars (Cortés-Contreras 2016; Schöfer et al. 2019), in which PM J09553–2715, PM J21463+3813, GI 699, GI 445, and GI 411 were identified as belonging to the thick disc, and GI 412A labelled as within the transition between thin and thick discs. Most other stars studied by Cortés-Contreras (2016) and included in our work were classified as belonging to the thin or young disc, with a few exceptions such as GI 880, GI 905, and GJ 1151, placed either in the thick of transition between thick and thin discs. One should note that the boundary between thin and thick disc from $[\alpha/Fe]$ remains fuzzy even for giants making it tricky to clearly split the stars of our sample into two distinct populations.

In subsequent works, we will perform a similar analysis with other models, such as PHOENIX, which will require to compute new grids of synthetic spectra for different $[\alpha/Fe]$ values, and with up-to-date line lists. As our models evolve, we will revise the modifications performed on the line lists and identify additional stellar features to use for our purposes. This will allow us to further investigate the differences between models, and to identify the modelling assumptions that are best suited to the computation of synthetic spectra of M dwarfs and cool stars. Additionally, we will try to perform the same kind of analysis on more active targets that were excluded from our sample, and on the pre-main-sequence stars also observed with SPIRou in the framework of the SLS. The spectra of such stars may be impacted by activity, with effects from the chromosphere (Hintz et al. 2019) or Zeemann broadening (Deen 2013) and radius inflation due to stronger magnetic fields (Feiden & Chaboyer 2013). This may require the addition of extra steps to the modelling process. Spots are indeed likely to be present at the surface of active targets, which may require implementing a two-temperature model to reproduce their spectra (Gully-Santiago et al. 2017).

ACKNOWLEDGEMENTS

We acknowledge funding from the European Research Council under the H2020 & innovation program (grant #740651 NewWorlds).

This work is based on observations obtained at the Canada–France–Hawaii Telescope (CFHT), which is operated by the National

Research Council (NRC) of Canada, the Institut National des Sciences de l'Univers of the Centre National de la Recherche Scientifique (CNRS) of France, and the University of Hawaii. The observations at the CFHT were performed with care and respect from the summit of Maunakea, which is a significant cultural and historic site.

This research used the SIMBAD data base (Wenger et al. 2000), operated at CDS, Strasbourg, France.

TM acknowledges financial support from the Spanish Ministry of Science and Innovation (MICINN) through the Spanish State Research Agency, under the Severo Ochoa Program 2020-2023 (CEX2019-000920-S) as well as support from the ACIISI, Consejería de Economía, Conocimiento y Empleo del Gobierno de Canarias and the European Regional Development Fund (ERDF) under grant with reference PROID2021010128. 777.

We acknowledge funding from the French National Research Agency (ANR) under contract number ANR18CE310019 (SPLASH). XD and AC acknowledge support in the framework of the Investissements d'Avenir program (ANR-15-IDEX-02), through the funding of the 'Origin of Life' project of the Grenoble-Alpes University.

DATA AVAILABILITY

The data used in this work were acquired in the context of the SLS, and will be publicly available at the Canadian Astronomy Data Center one year after the completion of the program.

REFERENCES

- Adibekyan V. Z. et al., 2013, *A&A*, 554, A44
 Allard F., Hauschildt P. H., 1995, *ApJ*, 445, 433
 Allard F., Homeier D., Freytag B., 2011, in Johns-Krull C., Browning M. K., West A. A., eds, ASP Conf. Ser. Vol. 448, 16th Cambridge Workshop on Cool Stars, Stellar Systems, and the Sun. Astron. Soc. Pac., San Francisco, p. 91
 Alvarez R., Plez B., 1998, *A&A*, 330, 1109
 Baraffe I., Homeier D., Allard F., Chabrier G., 2015, *A&A*, 577, A42
 Bonfils X. et al., 2013, *A&A*, 556, A110
 Boyajian T. S. et al., 2012, *ApJ*, 757, 112
 Cifuentes C. et al., 2020, *A&A*, 642, A115
 Cortés-Contreras M., 2016, PhD thesis, Univ. Complutense de Madrid
 Cristofari P. I. et al., 2022, *MNRAS*, 511, 1893 (C22)
 Deen C. P., 2013, *AJ*, 146, 51
 Donati J. F. et al., 2020, *MNRAS*, 498, 5684
 Dotter A., Chaboyer B., Jevremović D., Kostov V., Baron E., Ferguson J. W., 2008, *ApJS*, 178, 89
 Dressing C. D., Charbonneau D., 2013, *ApJ*, 767, 95
 Feiden G. A., Chaboyer B., 2012, *ApJ*, 757, 42
 Feiden G. A., Chaboyer B., 2013, *ApJ*, 779, 183
 Fouqué P. et al., 2018, *MNRAS*, 475, 1960
 Fuhrmann K., 1998, *A&A*, 338, 161
 Gaidos E., Mann A. W., Kraus A. L., Ireland M., 2016, *MNRAS*, 457, 2877
 Gully-Santiago M. A. et al., 2017, *ApJ*, 836, 200
 Gustafsson B., Edvardsson B., Eriksson K., Jørgensen U. G., Nordlund, Å., Plez B., 2008, *A&A*, 486, 951
 Hintz D. et al., 2019, *A&A*, 623, A136
 Husser T. O., Wende-von Berg S., Dreizler S., Homeier D., Reiners A., Barman T., Hauschildt P. H., 2013, *A&A*, 553, A6
 Ishikawa H. T., Aoki W., Kotani T., Kuzuhara M., Omiya M., Reiners A., Zechmeister M., 2020, *PASJ*, 72, 102
 Ishikawa H. T. et al., 2022, *AJ*, 163, 72
 Jackson R. J., Deliyannis C. P., Jeffries R. D., 2018, *MNRAS*, 476, 3245
 Jönsson H. et al., 2020, *AJ*, 160, 120
 Kotani T. et al., 2018, in Evans C. J., Simard L., Takami H., eds, Proc. SPIE Conf. Ser. Vol. 10702, Ground-based and Airborne Instrumentation for Astronomy VII. SPIE, Bellingham, p. 1070211
 Kurucz R. L., 1970, SAO Special Report, 309
 Kurucz R. L., 2005, *Memorie della Societa Astronomica Italiana Supplementi*, 8, 14
 Mahadevan S. et al., 2012, in McLean I. S., Ramsay S. K., Takami H., eds, Proc. SPIE Conf. Ser. Vol. 8446, Ground-based and Airborne Instrumentation for Astronomy IV. SPIE, Bellingham, p. 84461S
 Mann A. W., Brewer J. M., Gaidos E., Lépine S., Hilton E. J., 2013, *AJ*, 145, 52
 Mann A. W., Feiden G. A., Gaidos E., Boyajian T., von Braun K., 2015, *ApJ*, 804, 64 (M15)
 Mann A. W. et al., 2019, *ApJ*, 871, 63
 Marfil E. et al., 2021, *A&A*, 656, A162
 Neves V., Bonfils X., Santos N. C., Delfosse X., Forveille T., Allard F., Udry S., 2014, *A&A*, 568, A121
 Pakhomov Y. V., Ryabchikova T. A., Piskunov N. E., 2019, *Astron. Rep.*, 63, 1010
 Passegger V. M. et al., 2018, *A&A*, 615, A6
 Passegger V. M. et al., 2019, *A&A*, 627, A161
 Petit P. et al., 2021, *A&A*, 648, A55
 Plez B., 2012, Astrophysics Source Code Library, record ascl: 1205.004
 Press W. H., Teukolsky S. A., Vetterling W. T., Flannery B. P., 1992, *Numerical Recipes in C (2nd Ed.): The Art of Scientific Computing*. Cambridge University Press, USA
 Quirrenbach A. et al., 2014, in Ramsay S. K., McLean I. S., Takami H., eds, Proc. SPIE Conf. Ser. Vol. 9147, Ground-based and Airborne Instrumentation for Astronomy V. SPIE, Bellingham, p. 91471F
 Rajpurohit A. S., Allard F., Teixeira G. D. C., Homeier D., Rajpurohit S., Mousis O., 2018, *A&A*, 610, A19
 Rayner J. et al., 2016, in Evans C. J., Simard L., Takami H., eds, Proc. SPIE Conf. Ser. Vol. 9908, Ground-based and Airborne Instrumentation for Astronomy VI. SPIE, Bellingham, p. 990884
 Rojas-Ayala B., Covey K. R., Muirhead P. S., Lloyd J. P., 2010, *ApJ*, 720, L113
 Schöfer P. et al., 2019, *A&A*, 623, A44
 Schweitzer A. et al., 2019, *A&A*, 625, A68
 Souto D. et al., 2022, *ApJ*, 927, 123
 Unsold A., 1955, *Physik der Sternatmosphären*, MIT besonderer Berücksichtigung der Sonne. Springer-Verlag, Berlin
 Wenger M. et al., 2000, *A&AS*, 143, 9

SUPPORTING INFORMATION

Supplementary data are available at *MNRAS* online.

Figure S1. Best-fitting models obtained for five stars in our sample.

Please note: Oxford University Press is not responsible for the content or functionality of any supporting materials supplied by the authors. Any queries (other than missing material) should be directed to the corresponding author for the article.

APPENDIX A: FIGURES WITH LABELS

Figs A1 to A6 present alternative plots to Figs 1, 4, 5, 7, 8, and 9 with labels identifying the stars.

APPENDIX B: RESULTS ON CALIBRATION STARS

Figs B1 and B2 present a comparison of the results obtained with and without corrections applied to the line list parameters (see Section 5).

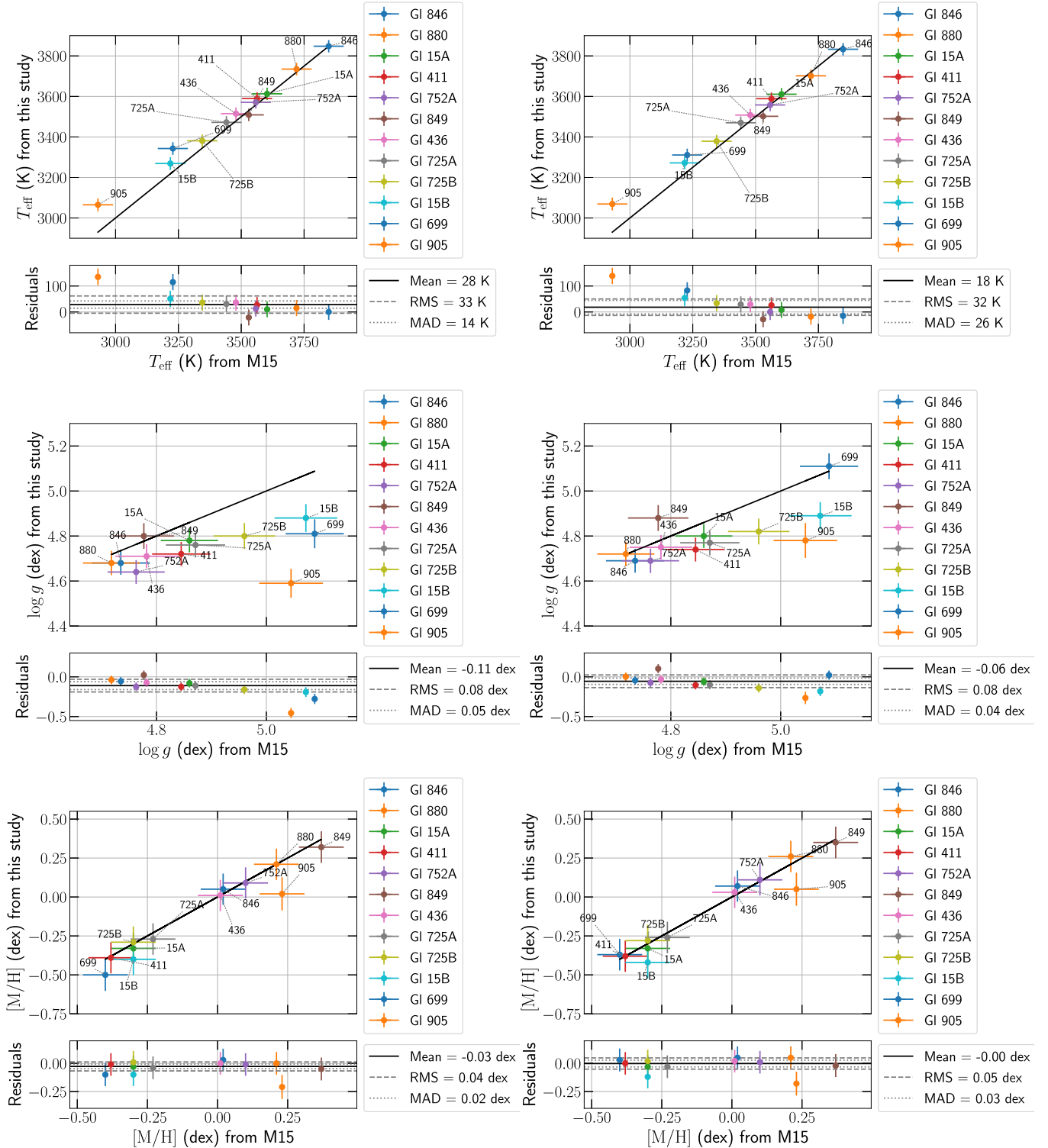


Figure B1. Comparisons between the retrieved T_{eff} , $\log g$, and $[M/H]$ for our 12 calibration stars. The left- and right-hand panels present the results obtained before and after the corrections applied to the line list parameters listed in Section 5.

Fig. B3 illustrates the effect of fitting on $[\alpha/\text{Fe}]$ on the retrieved parameters of our calibration stars.

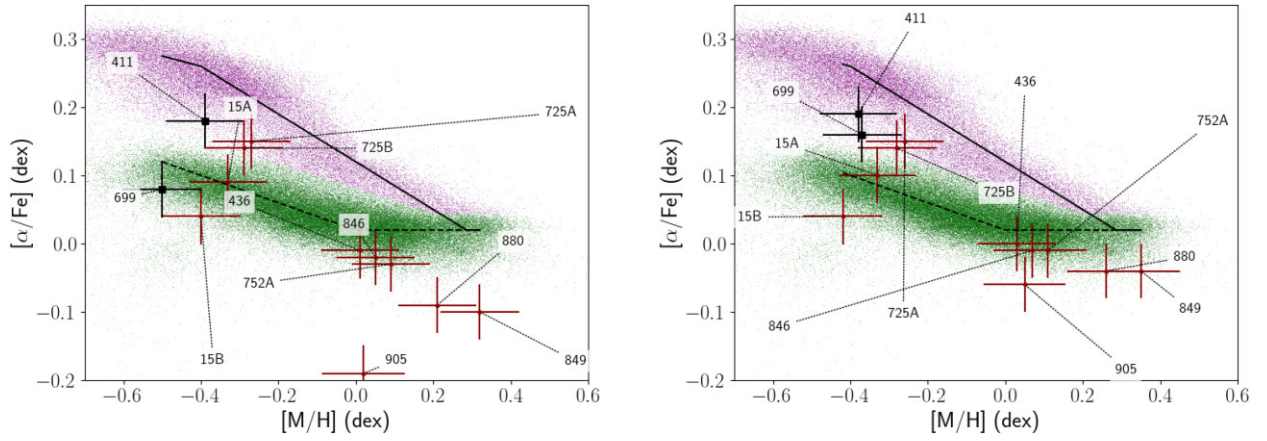


Figure B2. Retrieved $[\alpha/\text{Fe}]$ and $[\text{M}/\text{H}]$ values for our 12 calibration stars. The purple and green pixels depict APOGEE data for giants of the thick and thin disc, respectively. The stars in our sample expected to belong to the thick disc from their velocity are marked with a black square symbol. The solid and dashed black lines mark empirical thick and thin disc $[\text{M}/\text{H}]-[\alpha/\text{Fe}]$ relations, respectively. The left- and right-hand panels present the results obtained before and after correction on some line parameters (see Section 5), respectively.

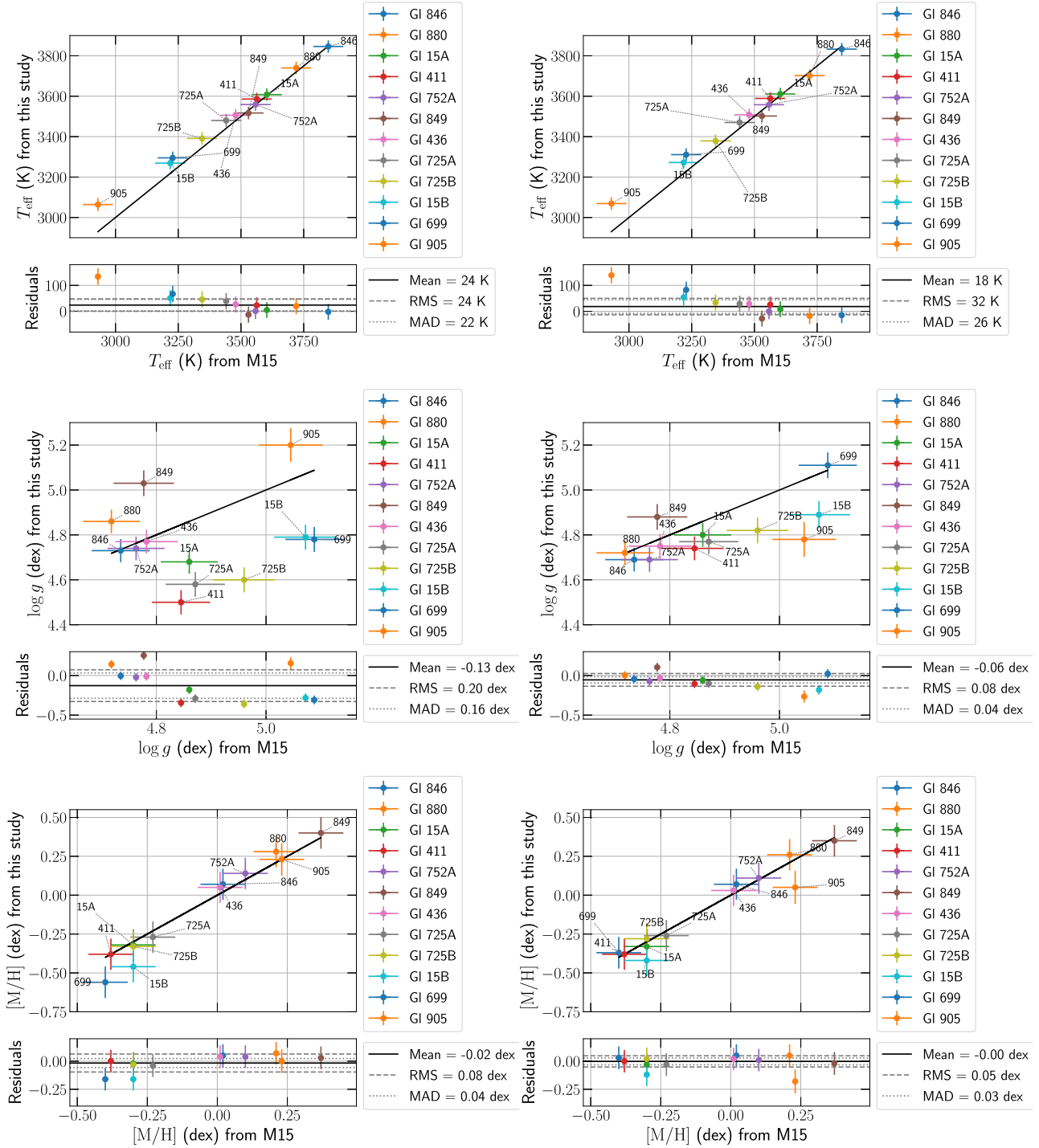


Figure B3. Same as Fig. B1 but comparing the results obtained with $[\alpha/\text{Fe}] = 0$ dex (left-hand panels) and while fitting $[\alpha/\text{Fe}]$ (right-hand panels). These results are obtained with corrections of the line list described in Section 5.

APPENDIX C: BEST FITS ON ALL SPECTRAL LINES

Fig. C1 available as supplementary material presents the best fits obtained for five stars in our sample.

APPENDIX D: LITERATURE PARAMETERS COMPARISON

We present comparisons of parameters recovered by several studies. Figs D1 and D2 present the results for 32 and 35 stars studied by Passegger et al. (2019) and Marfil et al. (2021), respectively.

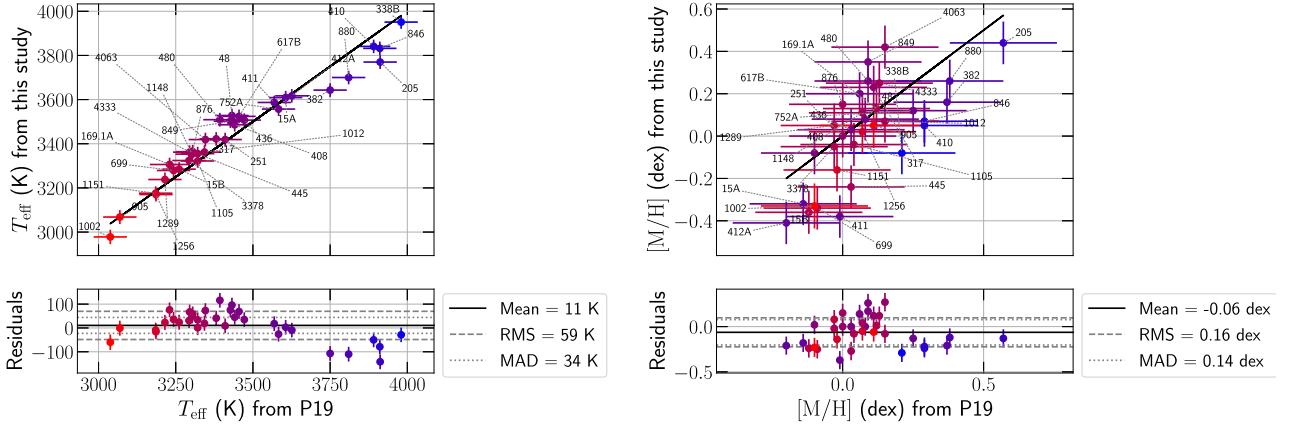


Figure D1. Comparison between retrieved parameters of 32 stars and the values published by Passegger et al. (2019).

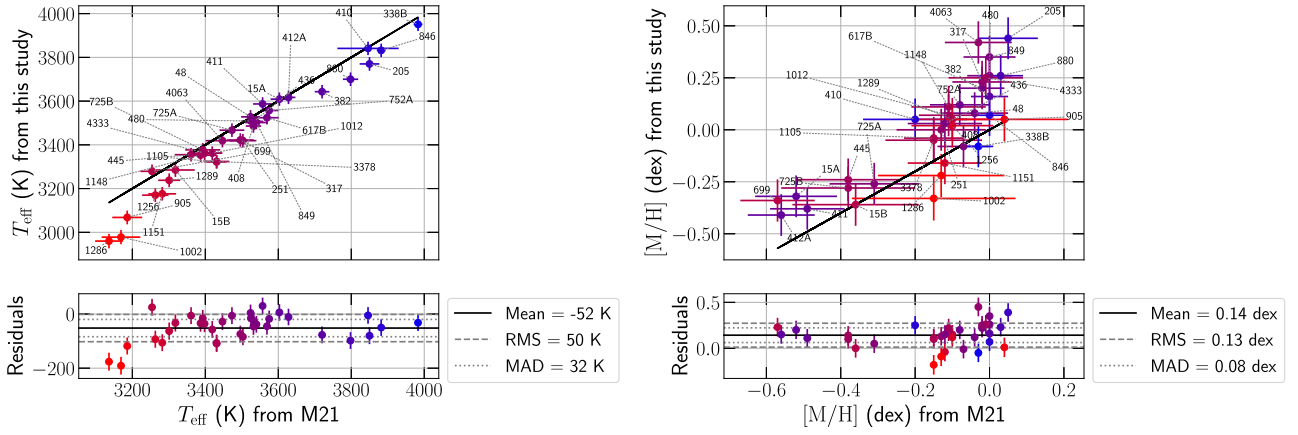


Figure D2. Same as Fig. D1 for 35 stars and values published by Marfil et al. (2021).

APPENDIX E: ESTIMATION OF LUMINOSITY

Fig. E1 presents a comparison between the luminosities estimated from G and J -band magnitudes using bolometric corrections (Cifuentes et al. 2020) and these reported by Cifuentes et al. (2020).

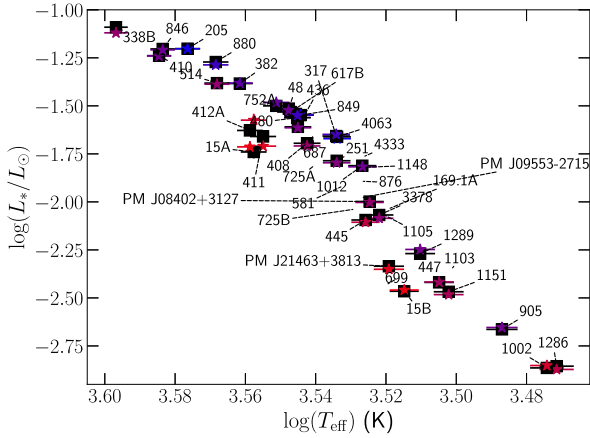


Figure E1. Comparison between the luminosities computed from bolometric corrections using the relation proposed by Cifuentes et al. (2020) (black squares), and those reported by Cifuentes et al. (2020) (coloured symbols) for 33 stars included in our sample. One should note that the T_{eff} values used by the authors to estimate the luminosities may differ from those estimated in this work. The symbol colours display the metallicity from low (red) to high (blue).

APPENDIX F: MASS–RADIUS RELATION

Fig. F1 presents a comparison between the masses and radii derived in this study and these reported by M15.

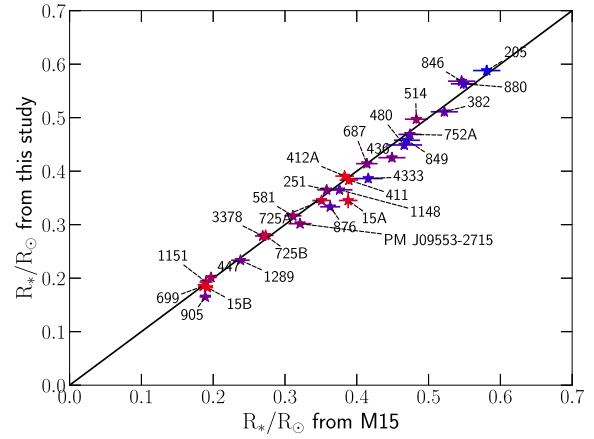
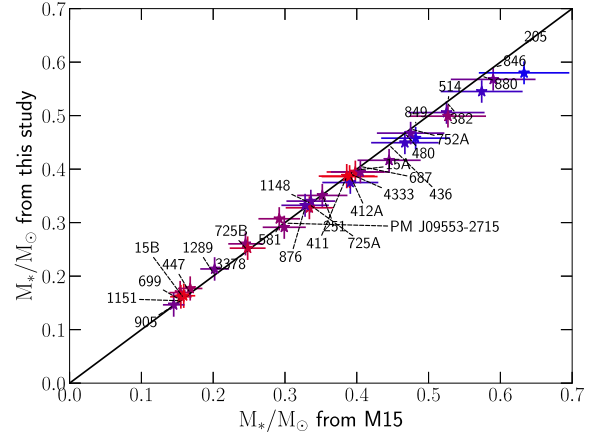


Figure F1. Comparison between our derived masses and radii and these reported by M15 for the 28 stars included in both studies (top and bottom panels, respectively). The black solid lines represent the equality.

This paper has been typeset from a \LaTeX file prepared by the author.